Supporting Information

Strongly Reducing (Diarylamino)benzene Based Covalent Organic Framework for Metal-Free Visible Light Photocatalytic H₂O₂ Generation

Chidharth Krishnaraj,[1,3] Himanshu Sekhar Jena,[1] Laurens Bourda,[1,2] Andreas Laemont,[1] Pradip Pachfule,[3] Jérôme Roeser,[3] C. Vinod Chandran,[4,5] Sander Borgmans,[6] Sven M. J. Rogge,[6] Karen Leus,[1] Christian V. Stevens,[7] Johan A. Martens,[4,5] Veronique Van Speybroeck,[6] Eric Breynaert,[4,5] Arne Thomas,[3*] and Pascal Van Der Voort[1*]

1. Section S1. General procedures

Materials. Unless stated otherwise all reagents were purchased from commercial sources and used without further purification.

Instrumentation. Fourier Transform Infrared Spectroscopy (FT-IR) in the region 4000-650 cm⁻¹ was performed with a Thermo Nicolet 6700 FTIR spectrometer equipped with a nitrogen-cooled MCT detector and a KBr beam splitter. Nitrogen adsorption-desorption isotherms were obtained using a Belsorp Mini apparatus measured at 77 K. Argon sorption was performed using micropore analyzer from 3P instruments. Elemental analyses (C, H, N and O) were carried out on a Thermo Scientific Flash 2000 CHNS-O analyzer equipped with a TCD detector. X-ray powder diffraction (XRPD) patterns were collected on a Thermo Scientific ARL X'Tra diffractometer, operated at 40 kV, 30 mA using Cu-Kα radiation (λ = 1.5406 Å). Thermogravimetric analysis (TGA) was performed on a Netzsch STA-449 F3 Jupiter-simultaneous TG-DSC analyzer within a temperature range of 20-800 °C, under a N_2 atmosphere and at a heating rate of 2 °C/min.

NMR spectroscopy: All the solid-state NMR experiments have been carried out in a Bruker 800 spectrometer operating at a ¹H Larmor frequency of 801.25 MHz at a magnetic field of 18.8 T equipped with a triple channel 1.9 mm magic-angle spinning (MAS) probe-head. The 1.9mm zirconia rotors were packed with the samples and spun at a MAS frequency of 35 kHz at room temperature (controlled by Bruker cooling unit). The ¹H NMR experiments were done with direct excitation with radio-frequency (RF) pulses of a strength of 140 kHz. Typically, eight transients were recorded with a recycle delay of 4 s for both samples. The ¹³C cross-polarization (CP) MAS experiments (Larmor frequency of 201.49 MHz) performed with varying contact times (1, 2, 4 and 8 ms) collected 4096 scans each. The decoupling sequence employed was SW$_f$-TPPM [S1] at an RF strength of 140 kHz. The 2D ¹³C-¹H CP-HETCOR experiment used a contact time of 2 ms with 320 transients and 80 incremented slices. The rotor-synchronized ¹H double-quantum-single-quantum (DQ-SQ) correlation experiments were performed with the standard BABA [S2, S3] sequence. The DQ excitation period was one rotor period and the duration for evolution of DQ coherence was incremented 120 times for the 2D experiment with 16 scans for each slice. The ¹H and ¹³C chemical shifts of the samples were referenced against corresponding shifts of tetramethylsilane (TMS).

2. Section S2. Synthesis of organic linkers and COFs

S2.1. Synthesis of 2,5-dimethylbenzene-1,4-dicarboxaldehyde [(Me)₂]
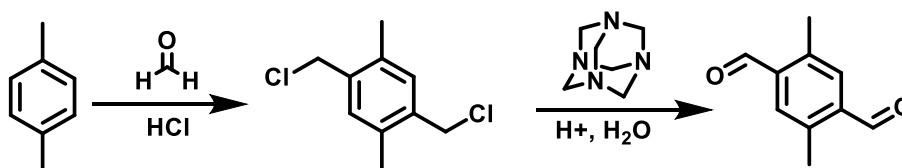
Scheme S1: Synthesis of 2,5-dimethylbenzene-1,4-dicarboxaldehyde [(Me)₂].

20 mL *p*-xylene (0.16 mol), 12.5 g *p*-formaldehyde (1.3 eq) and 13.6 g ZnCl (0.1 mol) were dissolved in 100 mL 37% HCl. The mixture was refluxed for 2 days at 110°C. Afterwards, the mixture was allowed to cool down to room temperature and the formed solid was filtered off to obtain 1,4-bis(chloromethyl)-2,5-dimethylbenzene as pure white needles. Yield = 25.27 g (77.8%). ¹H NMR (300 MHz, CDCl₃) δ 7.14 (s 2H), 4.55 (s 2H), 2.37 (s 6H).

1.446 g 1,4-bis(chloromethyl)-2,5-dimethylbenzene (7.1 mmol) and 2.6 g hexamine (18.6 mmol) were added to a 10 mL 50% acetic acid solution. The mixture was refluxed for 1h at 110°C, before addition of 5 mL 37% HCl.

Afterwards, reflux (110°C) was continued for 1 more hour, and the clear yellow mixture was subsequently cooled in an ice bath. 2,5-dimethylbenzene-1,4-dicarboxaldehyde crystallized out and was filtered off. (white flakes, yield = 83.4 %). ^{1}H NMR (300 MHz, CDCl$_3$) δ 10.34 (s 2H), 7.69 (s 2H), 2.70 (s 6H)
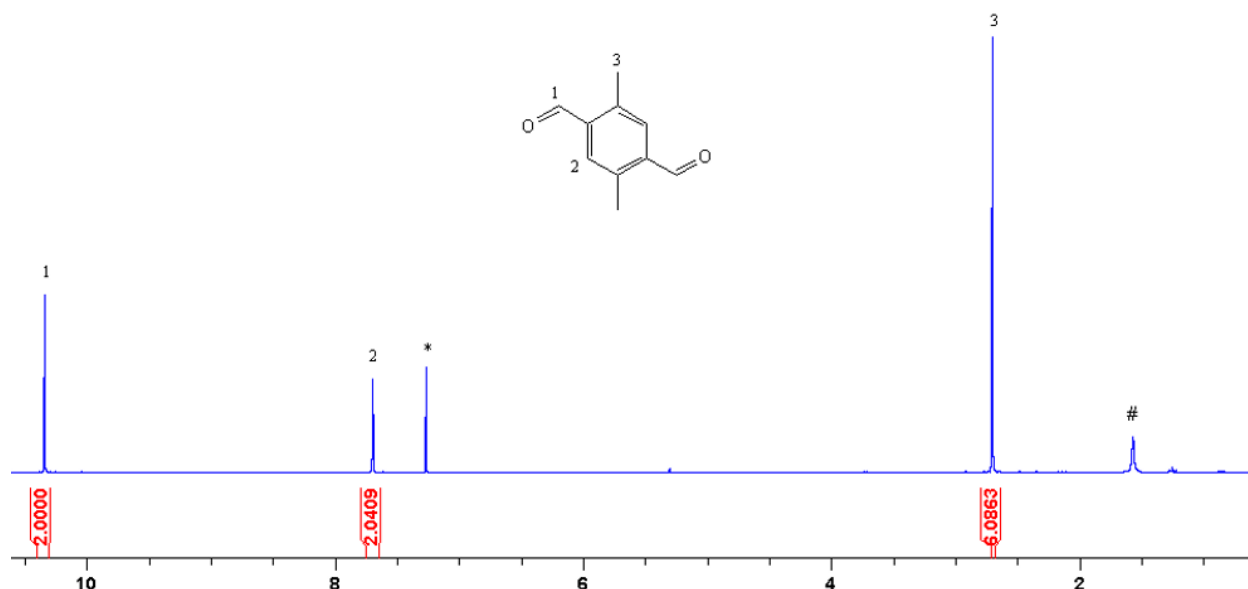
Figure S1: ^{1}H NMR spectra of 2,5-dimethylbenzene-1,4-dicarboxaldehyde, the solvent (CDCl$_3$) peak is depicted with *, the peak marked with # was assigned to residual H$_2$O in the sample.

S2.2. Synthesis of model compound TAPD-(Me)$_2$-MC
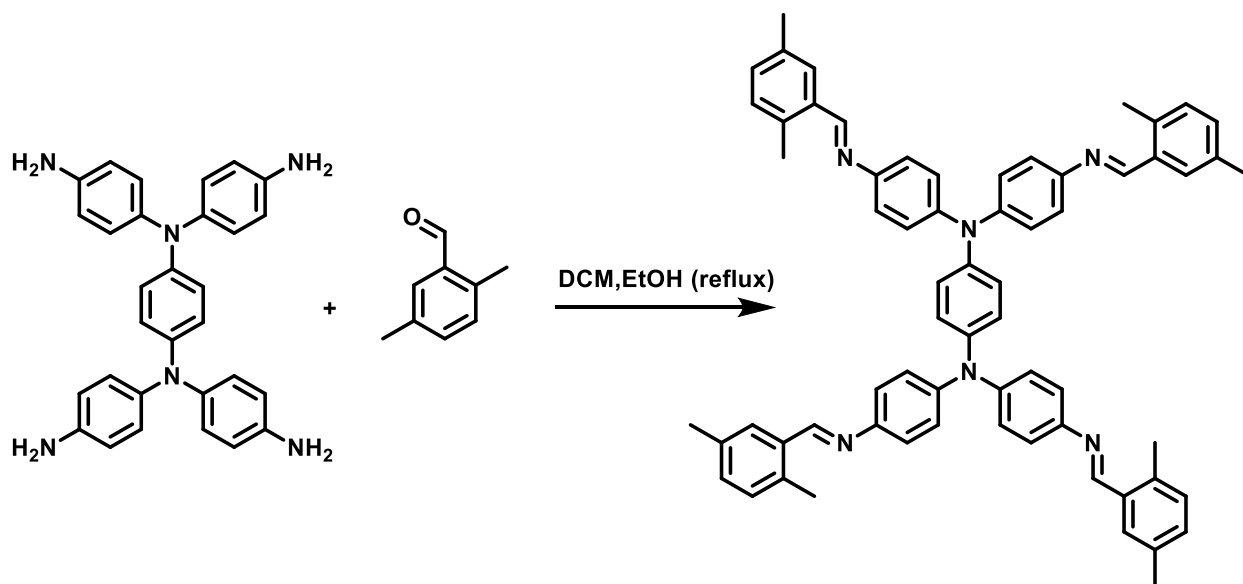
Scheme S2: Synthesis of model compound TAPD-(Me)$_2$-MC.

N,N,N',N'-Tetrakis(4-aminophenyl)-1,4-phenylenediamine (TAPD, 23.6 mg. 0.5 mmol) and 2,5-dimethylbenzene-1,4-dicarboxaldehyde ((Me)$_2$, 40.2 mg, 3 mmol) were added in a round bottom flask equipped with a magnetic stirring bar. 4 ml of dichloromethane and 4 ml of absolute ethanol were added to the mixture and

stirred under reflux for 5 hours. The reaction mixture was cooled to room temperature and the precipitate was filtered off. The orange-brown solid is washed thoroughly with ethanol and dried. Yield = 94%. 1H NMR (300 MHz, CDCl3) δ 8.71 (s 4H), 7.83 (s 4H), 6.99-7.11 (28H), 2.47 (s 12H), 2.30 (s 12H).

Figure S2: ^{1}H NMR spectra of model compound TAPD-(Me)$_2$-MC, the solvent (CDCl$_3$) peak is depicted with *, the peak marked with # was assigned to residual dichloromethane in the sample.
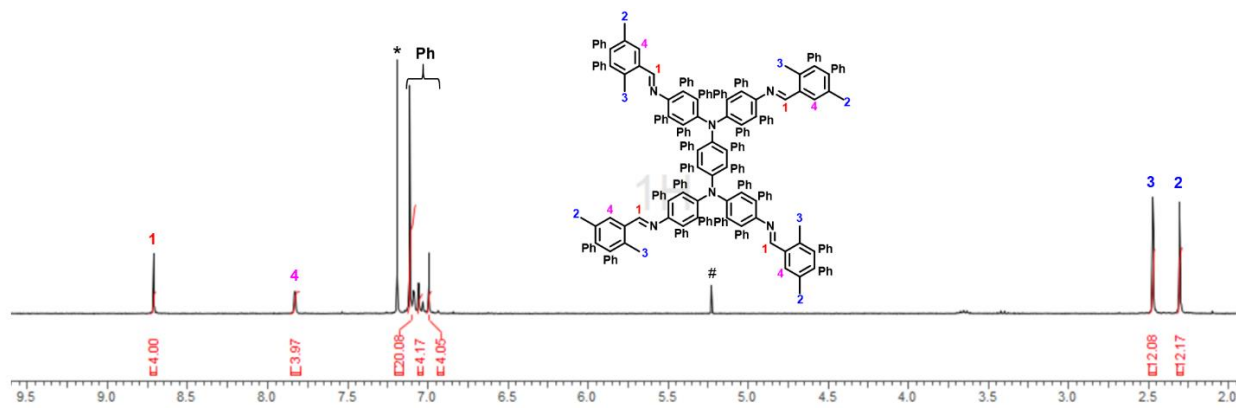
S2.3. Synthesis of model compound TAPD-(OMe)$_2$-MC

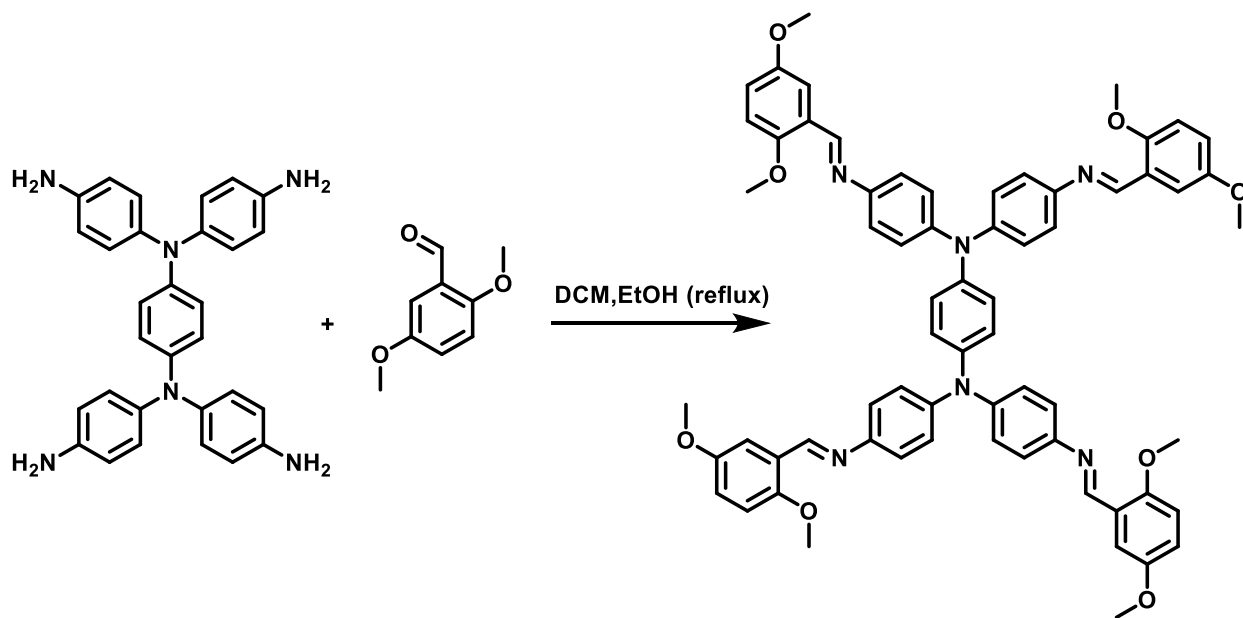**Scheme S3:** Synthesis of model compound TAPD-(OMe)$_2$-MC.

N,N,N',N'-Tetrakis(4-aminophenyl)-1,4-phenylenediamine (TAPD, 23.6 mg. 0.5 mmol) and 2,5-dimethoxybenzene-1,4-dicarboxaldehyde ((OMe)$_2$, 49.8 mg, 3 mmol) were added in a round bottom flask

equipped with a magnetic stirring bar. 4 ml of dichloromethane and 4 ml of absolute ethanol were added to the mixture and stirred under reflux for 5 hours. The reaction mixture was cooled to room temperature and the precipitate was filtered off. The brown solid is washed thoroughly with ethanol and dried. Yield = 80%. 1H NMR (300 MHz, CDCl3) δ 8.86 (s 4H), 7.63 (d 4H), 6.81-7.16 (28H), 3.79 (d 24H).

Figure S3: ^{1}H NMR spectra of model compound TAPD-(OMe)$_2$-MC, the solvent (CDCl$_3$) peak is depicted with *, the peak marked with # was assigned to residual dichloromethane in the sample.

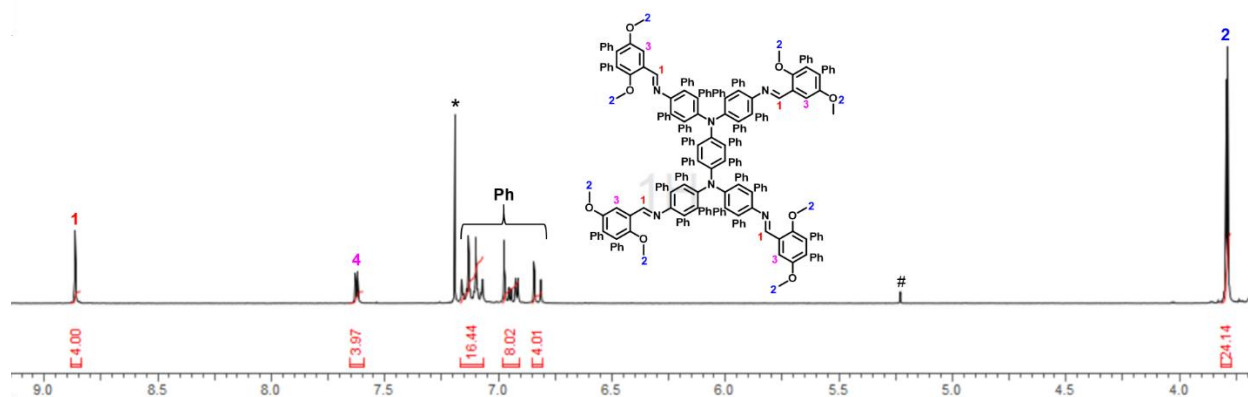### S2.4. Synthesis of TAPD-(Me)$_2$ COF

N,N,N',N'-Tetrakis(4-aminophenyl)-1,4-phenylenediamine (TAPD, 23.6 mg. 0.5 mmol) and 2,5-dimethylbenzene-1,4-dicarboxaldehyde ((Me)$_2$, 16.2 mg, 1 mmol) were added in an ampoule. 0.3 ml dichlorobenzene and 0.3 ml n-butanol were added to the ampoule. Finally, 0.1 ml 6M acetic acid was added, and the mixture was sonicated for 5 minutes. Freeze-pump-thaw procedure for 3 cycles were repeated before sealing the ampoule. The sealed ampoule was placed in an oven at 120°C. After 72 hours, the precipitate was filtered and washed with distilled water, tetrahydrofuran (THF) and acetone. The bright red solid is then washed using Soxhlet with THF for 12 hours. After drying the materials at 90°C for 24 h under vacuum **TAPD-(Me)$_2$ COF** (~38 mg) was obtained as bright red colored solid.

S2.5. Synthesis of TAPD-(OMe)$_2$ COF

N,N,N',N'-Tetrakis(4-aminophenyl)-1,4-phenylenediamine (TAPD, 23.6 mg. 0.5 mmol) and 2,5-dimethoxybenzene-1,4-dicarboxaldehyde ((OMe)$_2$, 19.4 mg, 1 mmol) were added in an ampoule. 0.3 ml mesitylene and 0.3 ml dioxane were added to the ampoule. Finally, 0.1 ml 6M acetic acid was added, and the mixture was sonicated for 5 minutes. Freeze-pump-thaw procedure for 3 cycles were repeated before sealing the ampoule. The sealed ampoule was placed in an oven at 120°C. After 72 hours, the precipitate was filtered and washed with distilled water, tetrahydrofuran (THF) and acetone. The dark red solid is then washed using Soxhlet with THF for 12 hours. After drying the materials at 90°C for 24 h under vacuum **TAPD-(OMe)$_2$ COF** (~42 mg) was obtained as dark red colored solid.

3. **Section S3: Characterization of COFs**

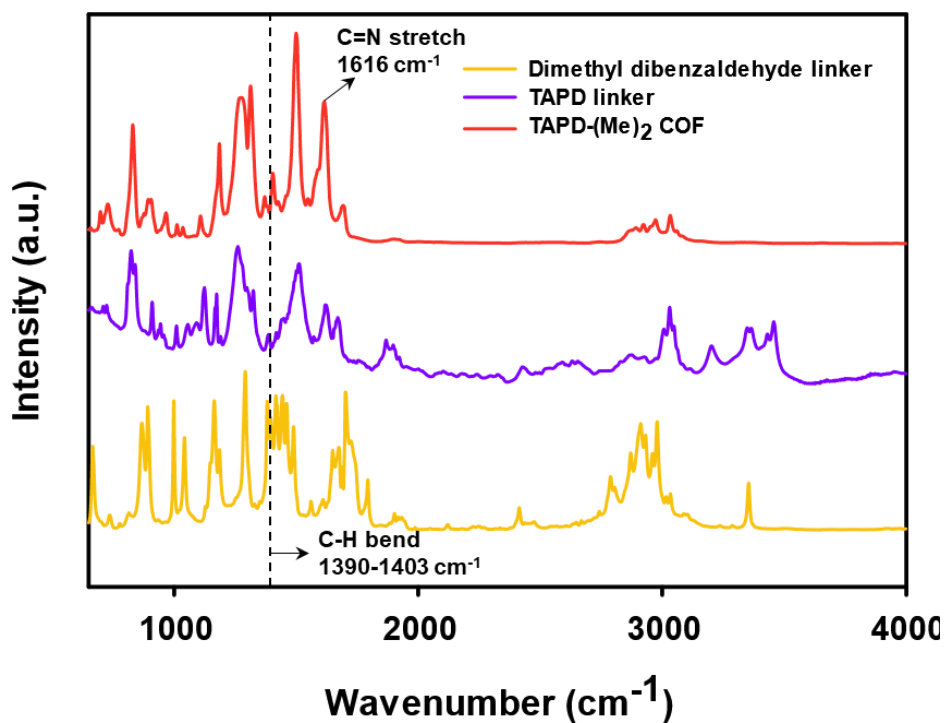**Figure S4:** FT-IR spectra of TAPD-$(Me)_2$ COF, TAPD linker and $(Me)_2$ linker.
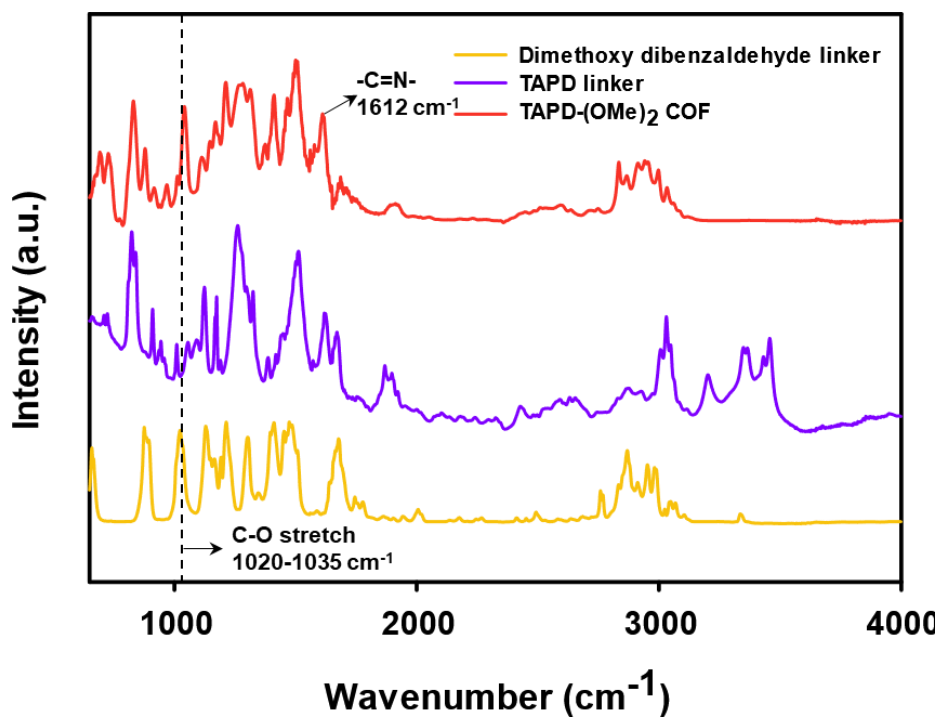
Figure S5: FT-IR spectra of TAPD-$(OMe)_2$ COF, TAPD linker and $(OMe)_2$ linker.

^{1}H DQ-SQ MAS (35 kHz) NMR

COF-Me
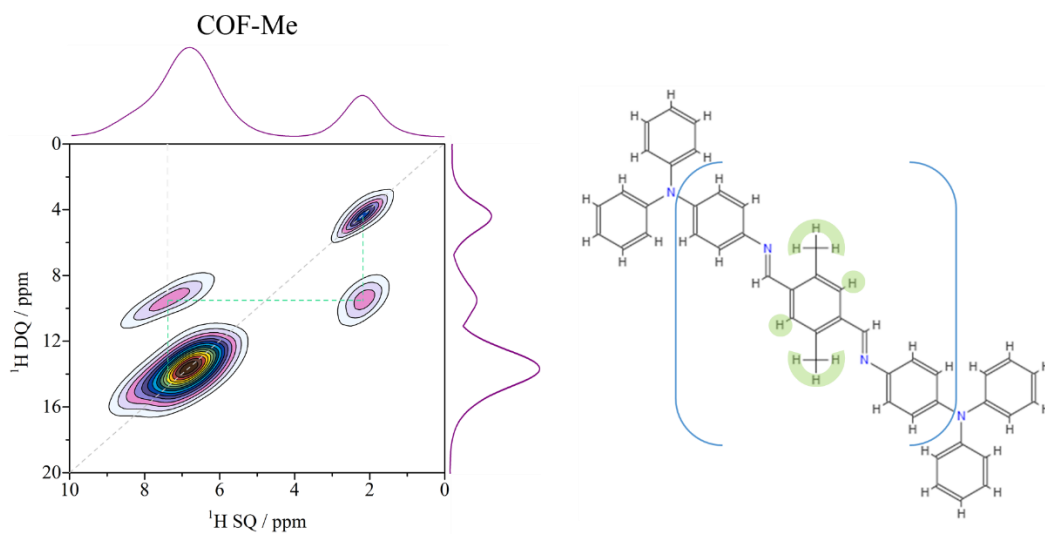
Figure S6. ^{1}H DQSQ correlation and assignment of TAPD-(Me)$_2$ COF.

^{1}H DQ-SQ MAS (35 kHz) NMR

COF-OMe
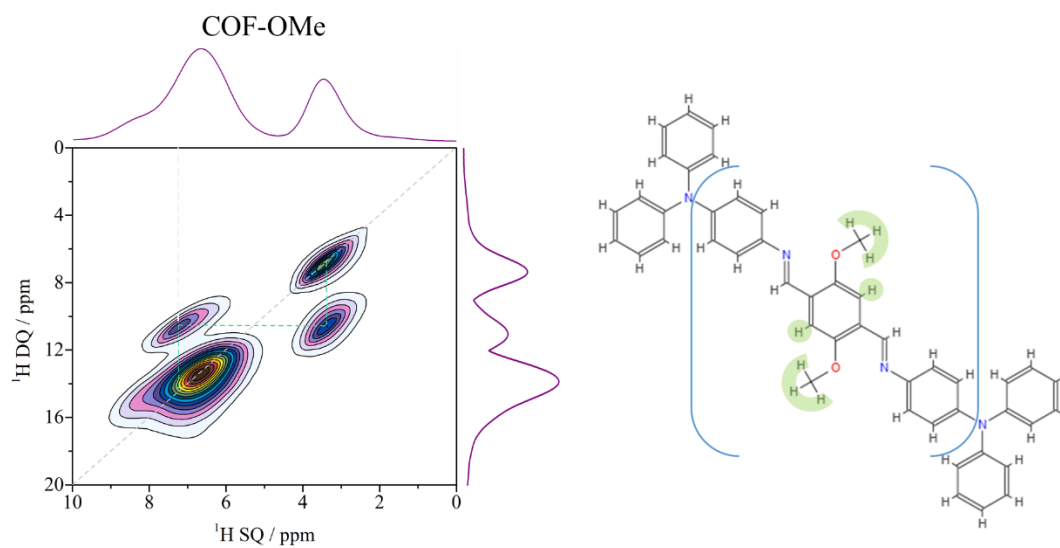
Figure S7. ^{1}H DQSQ correlation and assignment of TAPD-(OMe)$_2$ COF.
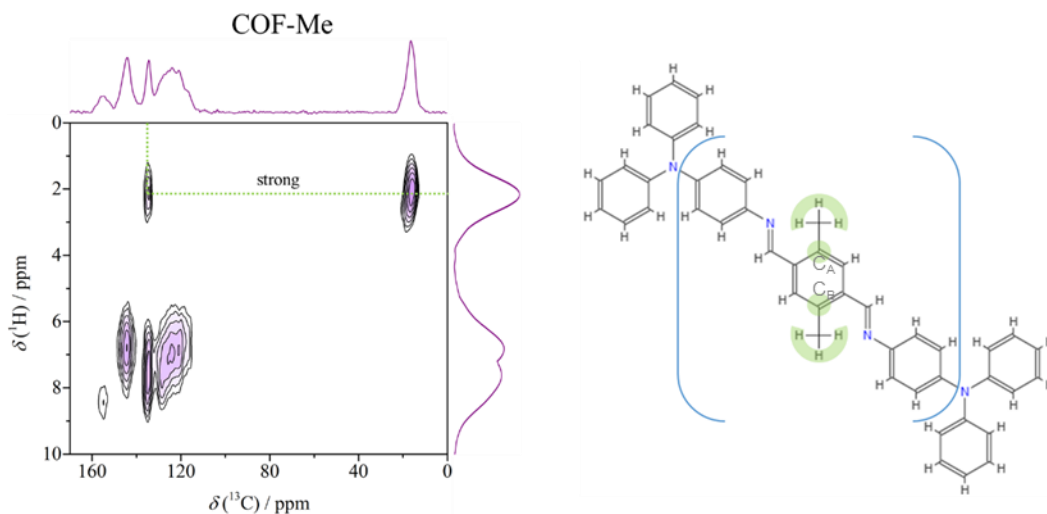
Figure S8. ^{1}H-^{13}C CP HETCOR spectrum and assignment TAPD-(Me)$_2$ COF.
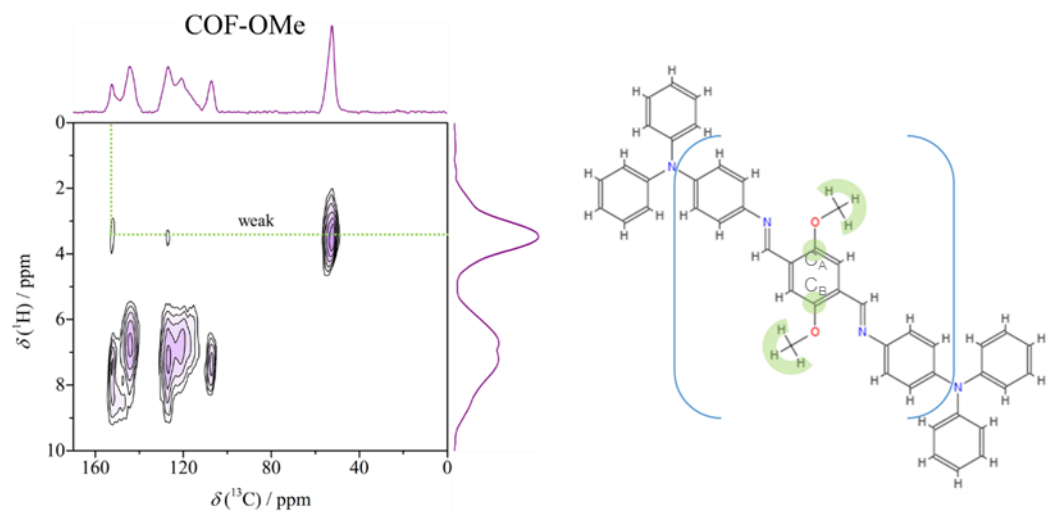
Figure S9. ^{1}H-^{13}C CP HETCOR spectrum and assignment of TAPD-(OMe)$_2$ COF.
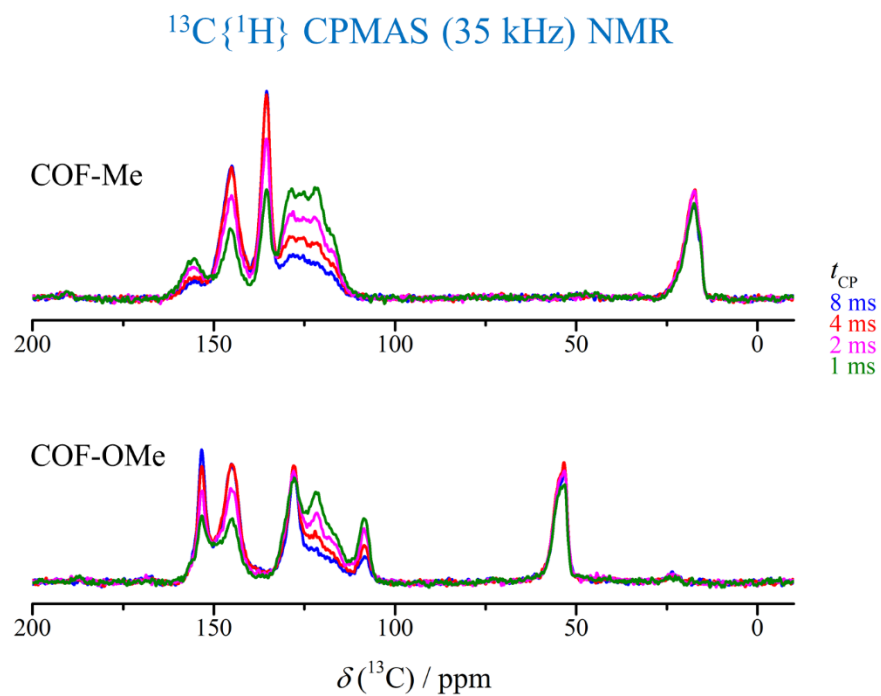
Figure S10. [1]H-^{13}C variable contact time CP buildup of TAPD-(Me)$_2$ COF (top) and TAPD-(OMe)$_2$ COF (bottom).
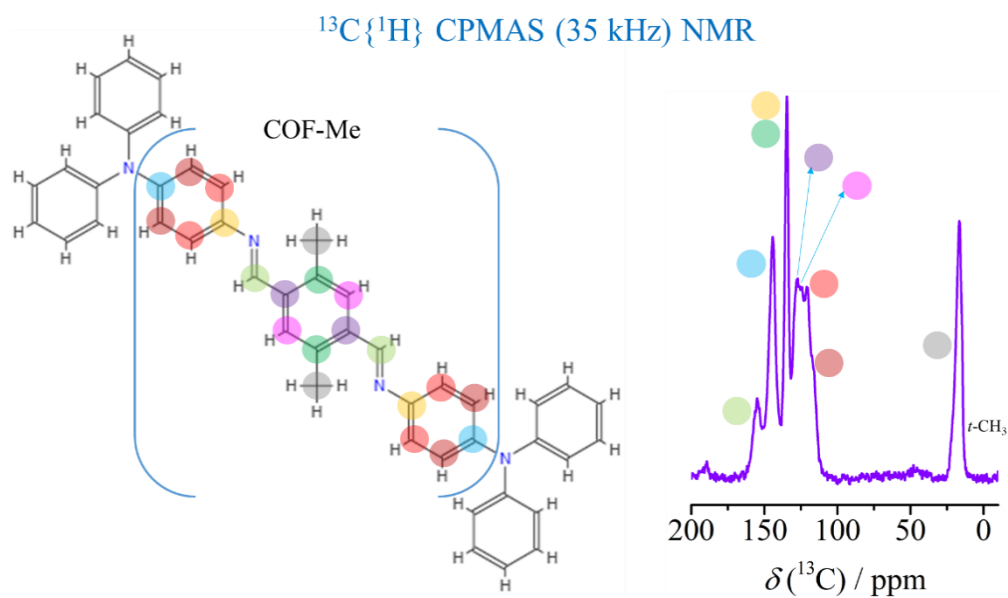
Figure S11. ^{1}H-^{13}C CPMAS (35 kHz) NMR spectrum (contact time 2 ms) and assignment of TAPD-(Me)$_2$ COF.
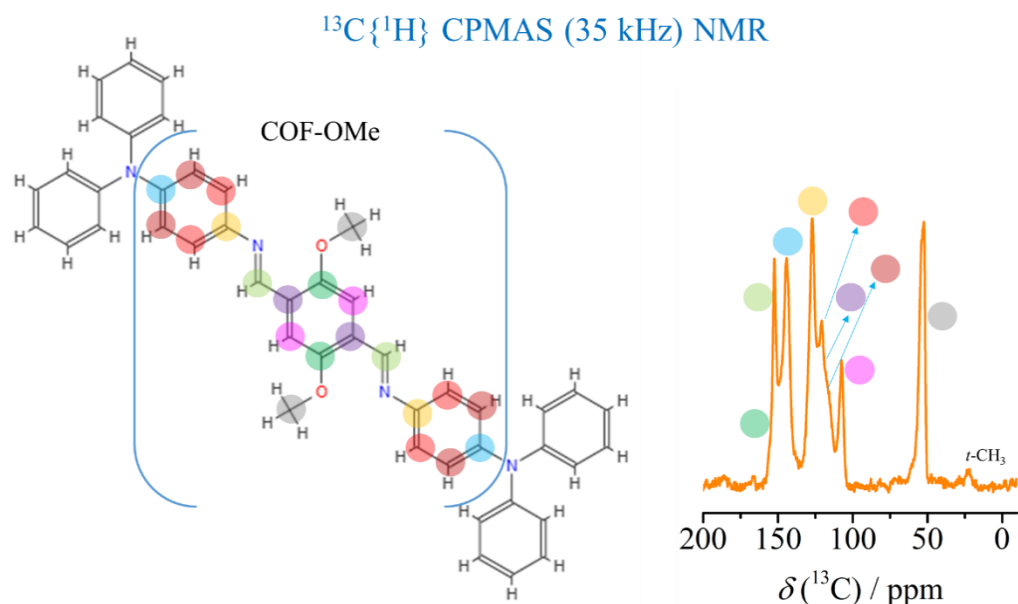
Figure S12. ^{1}H-^{13}C CPMAS (35 kHz) NMR spectrum (contact time 2 ms) and assignment of TAPD-(OMe)$_2$ COF.
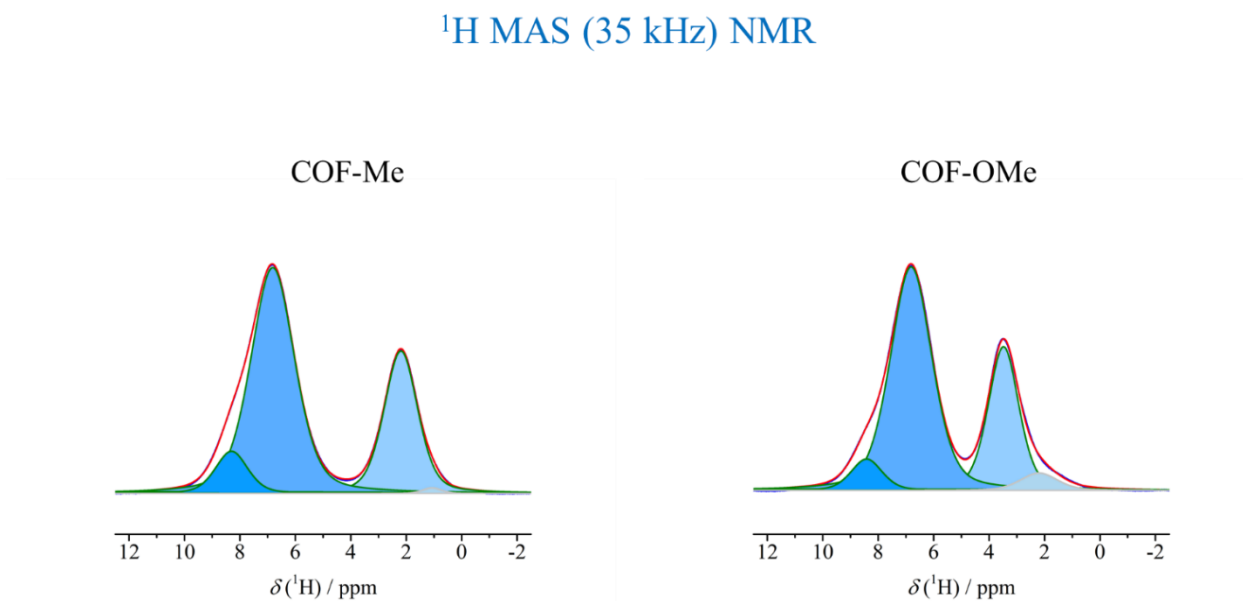
Figure S13. ^{1}H MAS (35 kHz) NMR spectra (and their decomposition) of TAPD-(Me)$_2$ COF (left) and TAPD-(OMe)$_2$ COF (right).

Table S1. Listed are the chemical shift, population, and assignment of TAPD-$(Me)_2$ COF and TAPD-$(OMe)_2$ COF

Material	Chemical shift / ppm	Population (%)	Assignment
TAPD-$(Me)_2$ COF	8.30	8.5	N=CH-Ph
	6.82	61.2	Ph-H
	2.20	29.7	-CH$_3$
	1.07	0.6	impurity
TAPD-$(OMe)_2$ COF	8.42	6.4	N=CH-Ph
	6.81	60.6	Ph-H
	3.48	28.8	-OCH$_3$
	2.20	4.21	-CH$_3$

Table S2: Elemental analysis of the TAPD COFs

Sample	C %	N %	H %	O %	C/N ratio	C/H ratio
TAPD-$(Me)_2$ COF – Exp	79.51	10.85	5.89	-	7.32	13.49
TAPD-$(Me)_2$ COF – Theory	82.84	11.59	5.56	-	7.15	14.89
TAPD-$(OMe)_2$ COF – Exp	72.19	9.72	5.19	-	7.42	13.90
TAPD-$(OMe)_2$ COF – Theory	69.75	9.76	5.62	14.87	7.15	12.41
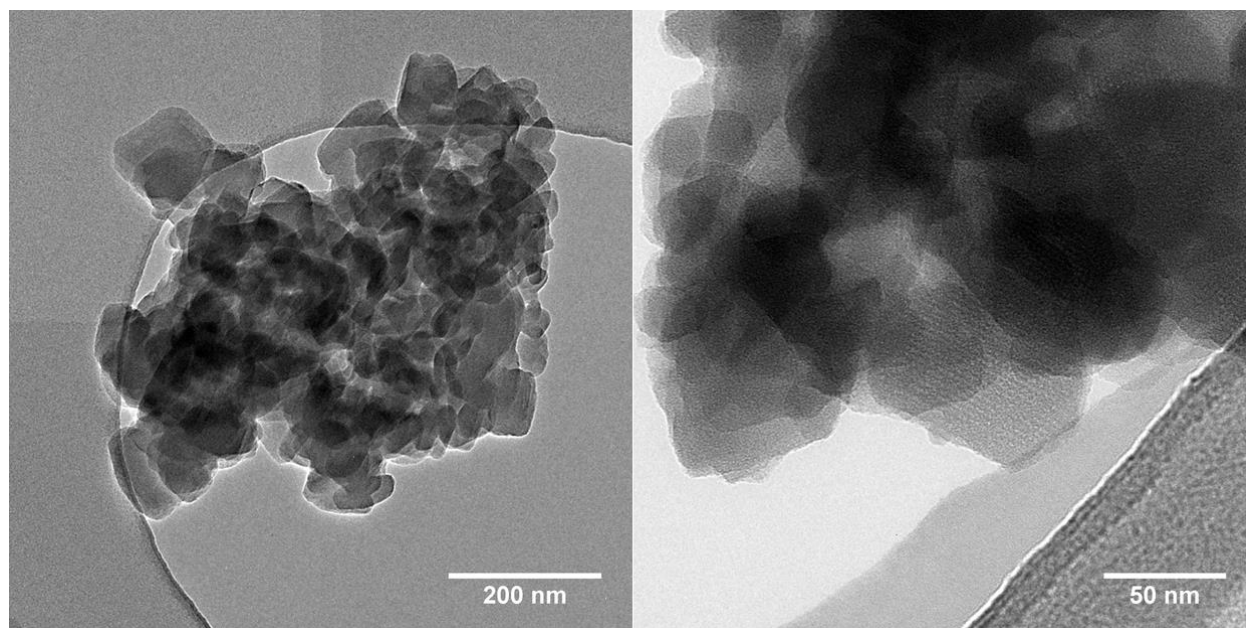
Figure S14: TEM images of TAPD-(Me)$_2$ COF showing layered structures.
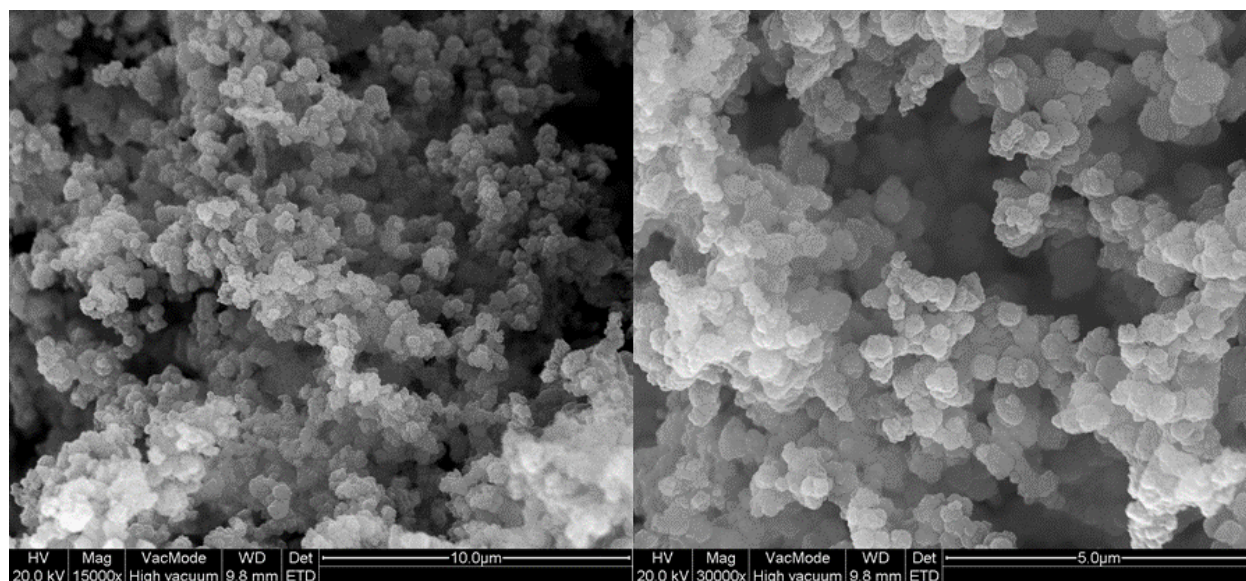
Figure S15: SEM images of TAPD-(Me)$_2$ COF showing homogeneous morphologies.
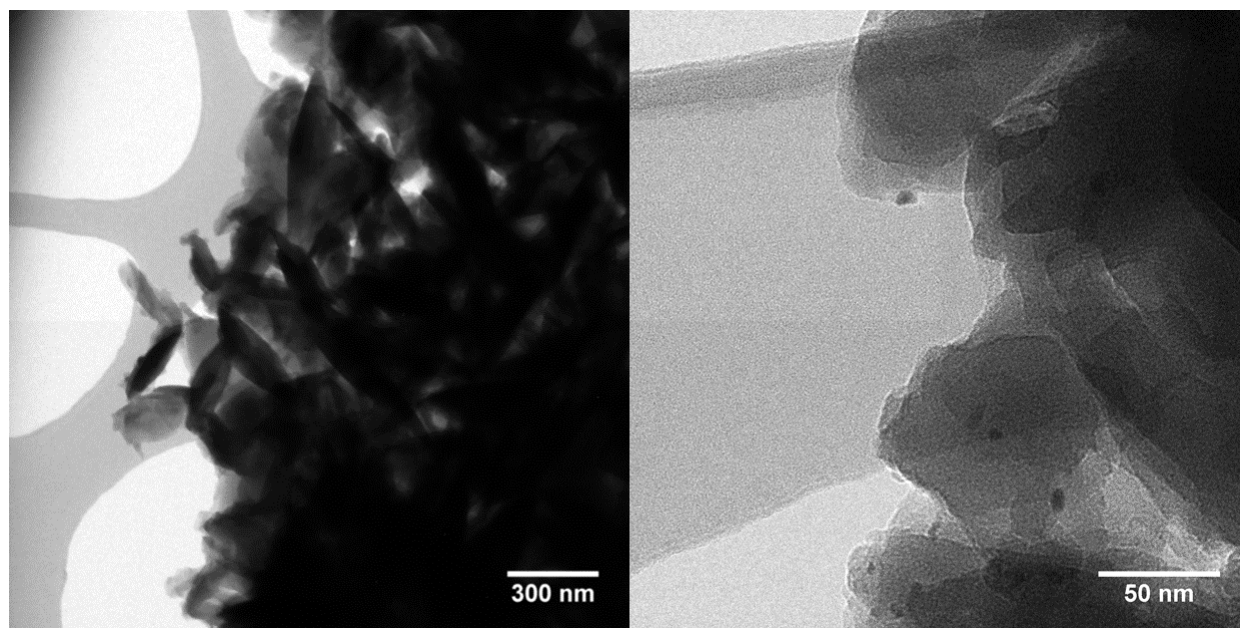
Figure S16: TEM images of TAPD-(OMe)$_2$ COF showing layered structures.
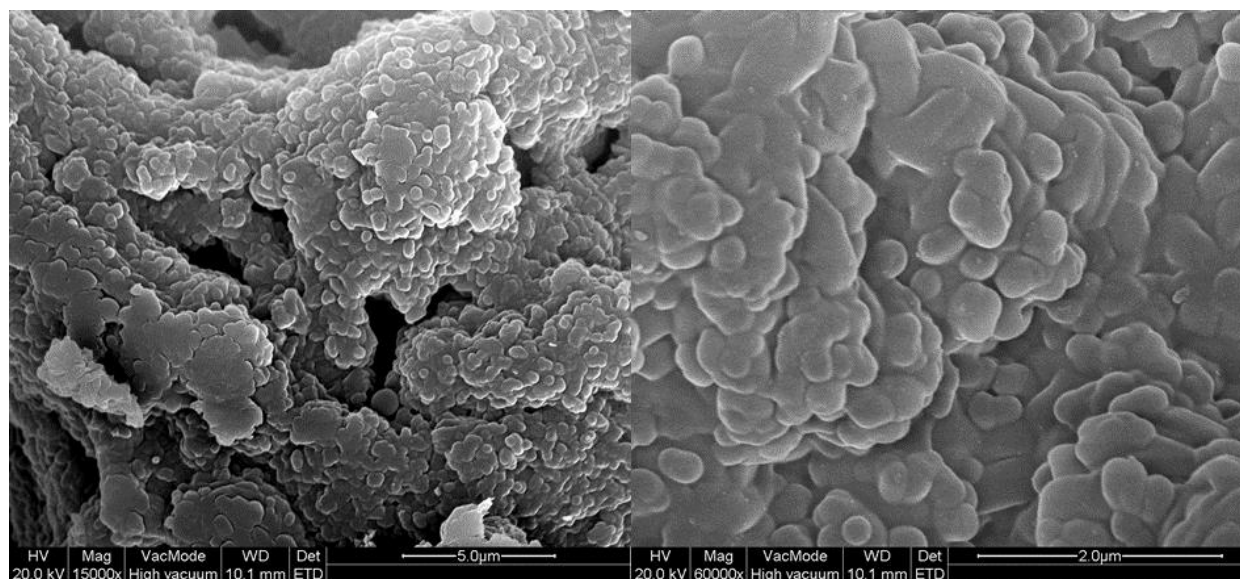
Figure S17: SEM images of TAPD-(OMe)$_2$ COF showing homogeneous morphologies.
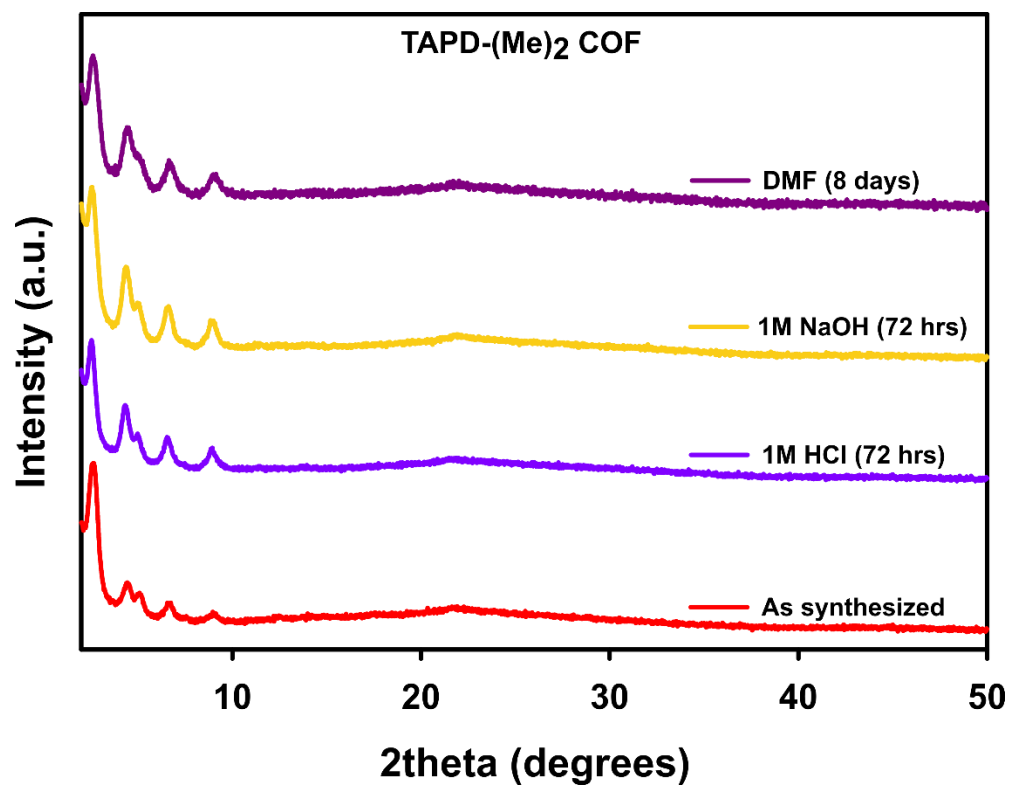
Figure S18: PXRD patterns of TAPD-(Me)$_2$ COF after treatment under different conditions.
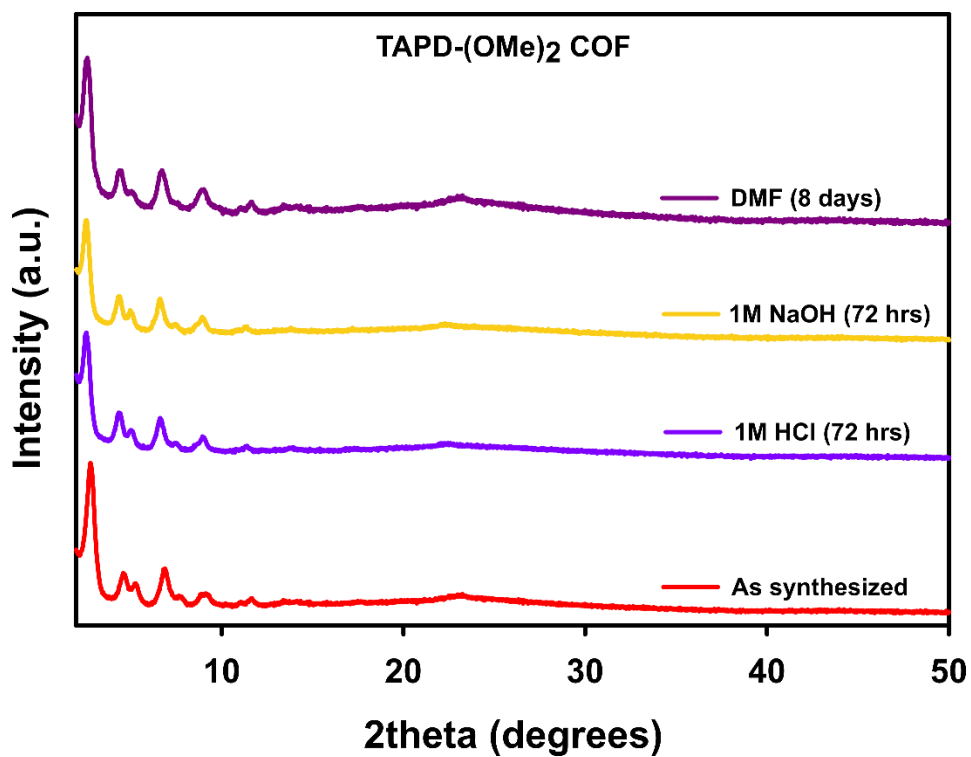
Figure S19: PXRD patterns of TAPD-(OMe)$_2$ COF after treatment under different conditions.
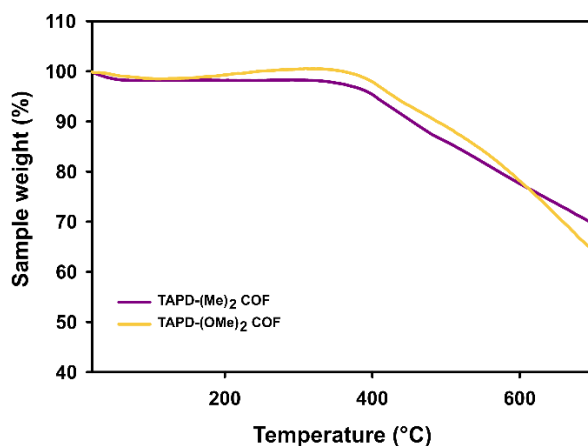
Figure S20: Thermogravimetric (TGA) spectra of TAPD-$(Me)_2$ and TAPD-$(OMe)_2$ COFs.

4. <u>Section S4: Structural modelling and atomic coordinates of COFs</u>

The structural crystal models with **kgm** topology of the TAPD-$(Me)_2$ and TAPD-$(OMe)_2$ COFs were initially constructed in a P6 primitive hexagonal unit cell in the Materials Studio suite of programs by Accelrys. Geometry optimization of the structures with Universal Force Field (UFF) led to satisfactory models whose theoretical pattern matched well the experimentally obtained patterns in terms of reflection positions and relative intensities. The Pawley profile refinements were performed using a Pseudo-Voigt profile function. The observed diffraction patterns were subjected to a polynomial background subtraction and the refined parameters included the zero point shift, the unit cell parameters, the FWHM parameters and the peak asymmetry (Berar-Baldizzoni function). For both the COFs, AA stacking and AB stacking models were constructed, and their corresponding PXRD patterns were calculated.

S4.1. Crystal Structure Data of TAPD-$(Me)_2$ COF
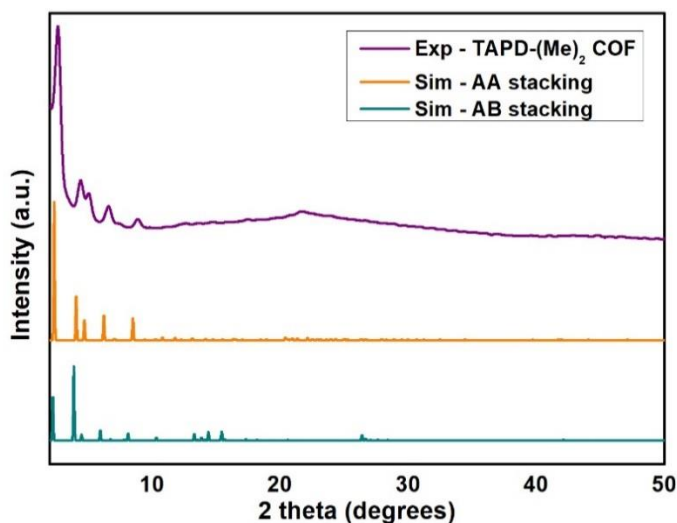
Figure S21: Simulated and experimental XRD patterns of TAPD-$(Me)_2$ COF; Cu-Kα radiation (λ = 1.5406 Å).
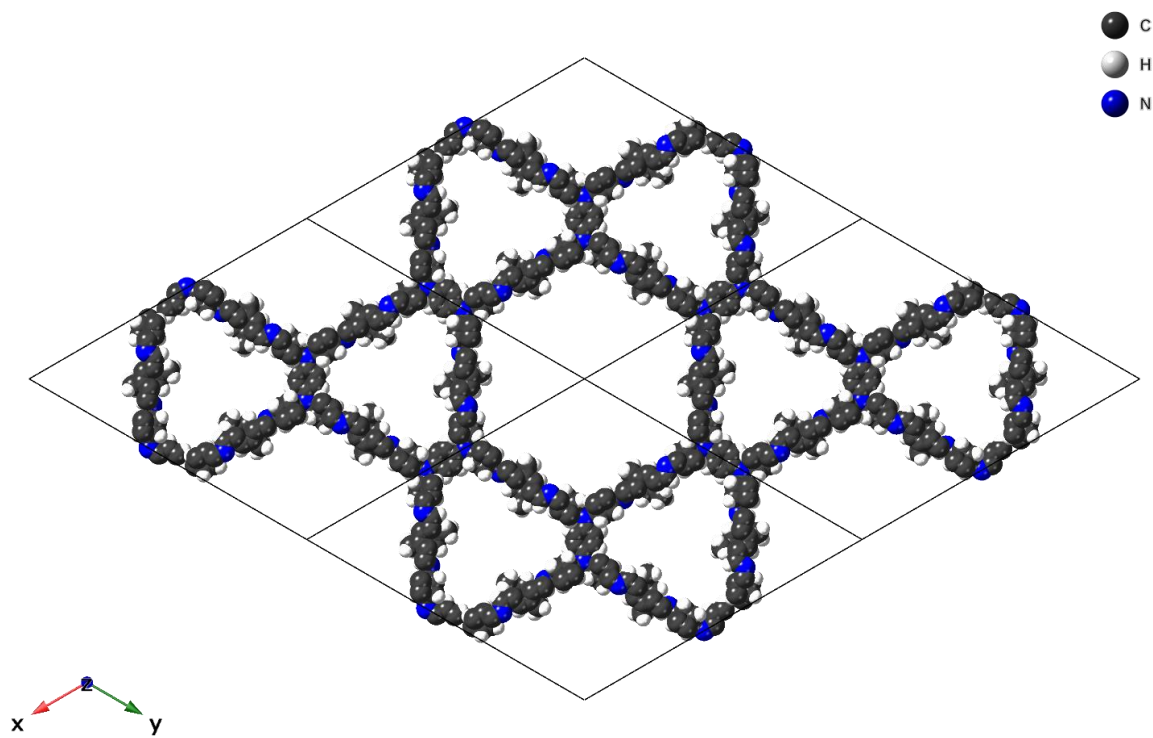
Figure S22: Theoretical structure of TAPD-(Me)$_2$ COF with eclipsed (AA) stacking arrangement.
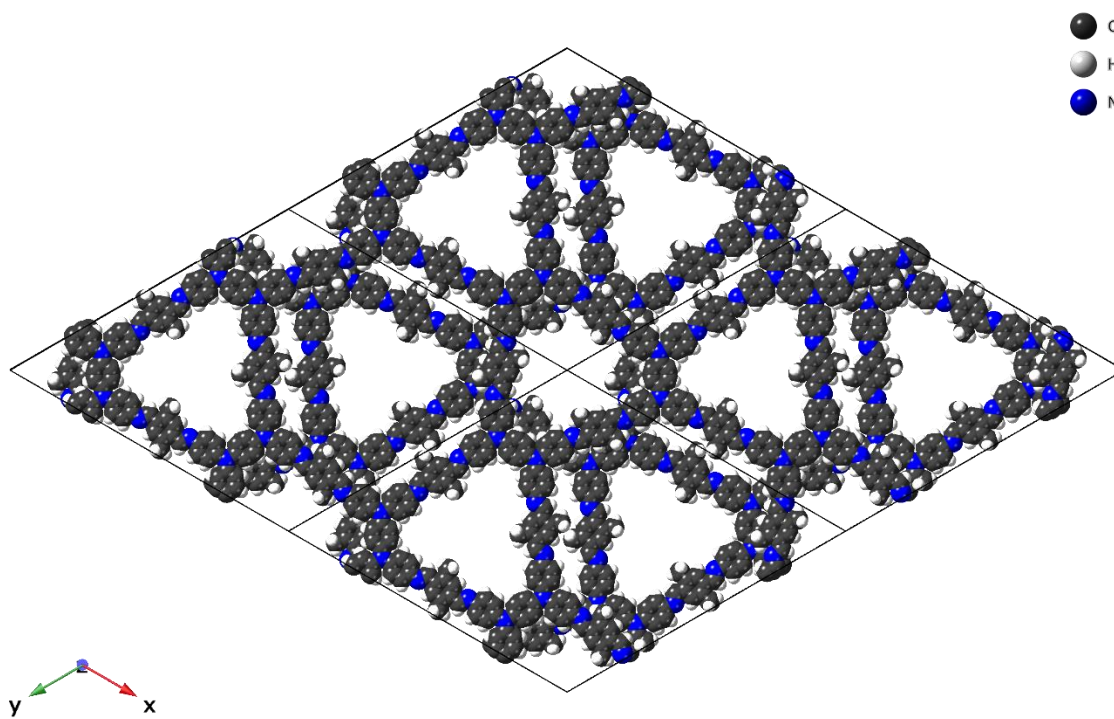
Figure S23: Theoretical structure of TAPD-(Me)₂ COF with eclipsed (AB) stacking arrangement.

S4.2. Crystal Structure Data of TAPD-(OMe)₂ COF
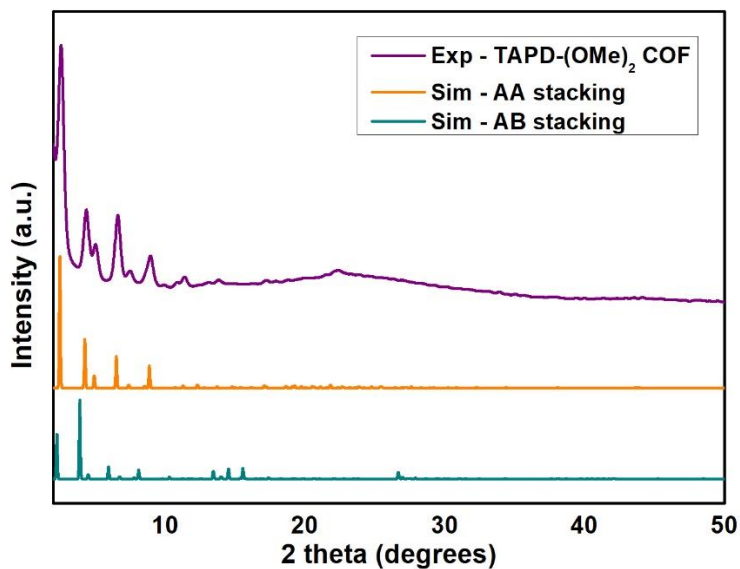
Figure S24: Simulated and experimental XRD patterns of TAPD-(OMe)₂ COF; Cu-Kα radiation (λ = 1.5406 Å).
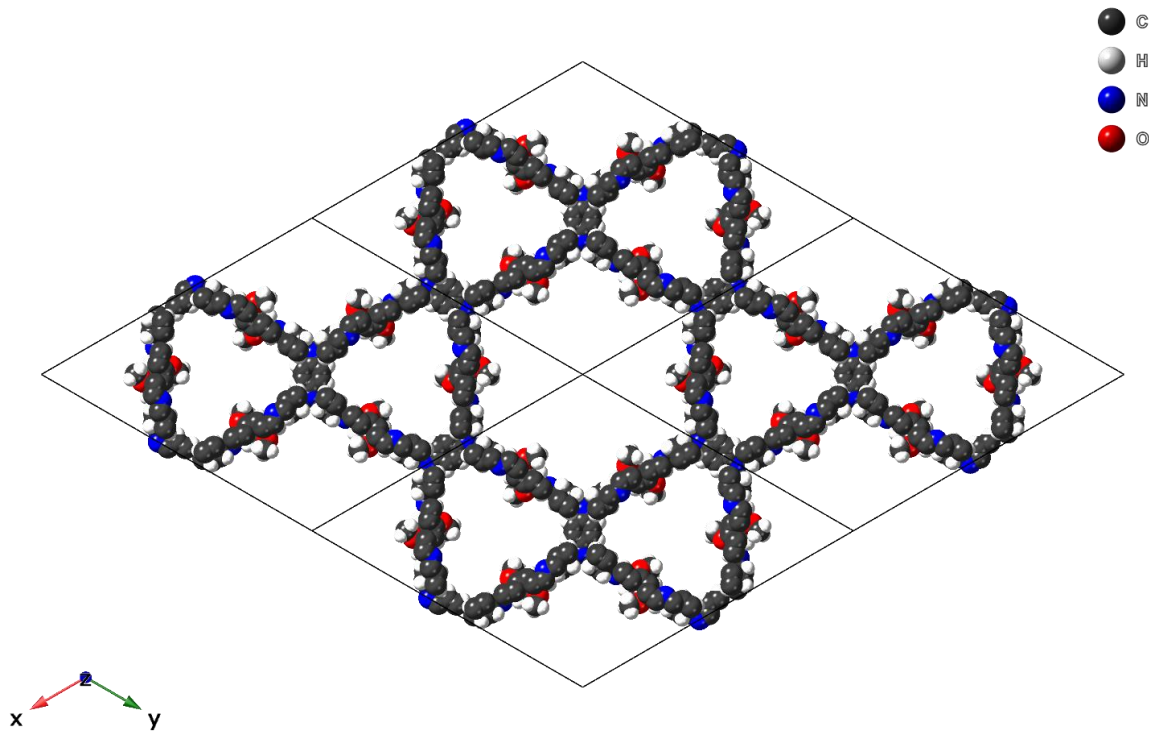
Figure S25: Theoretical structure of TAPD-(OMe)₂ COF with eclipsed (AA) stacking arrangement.
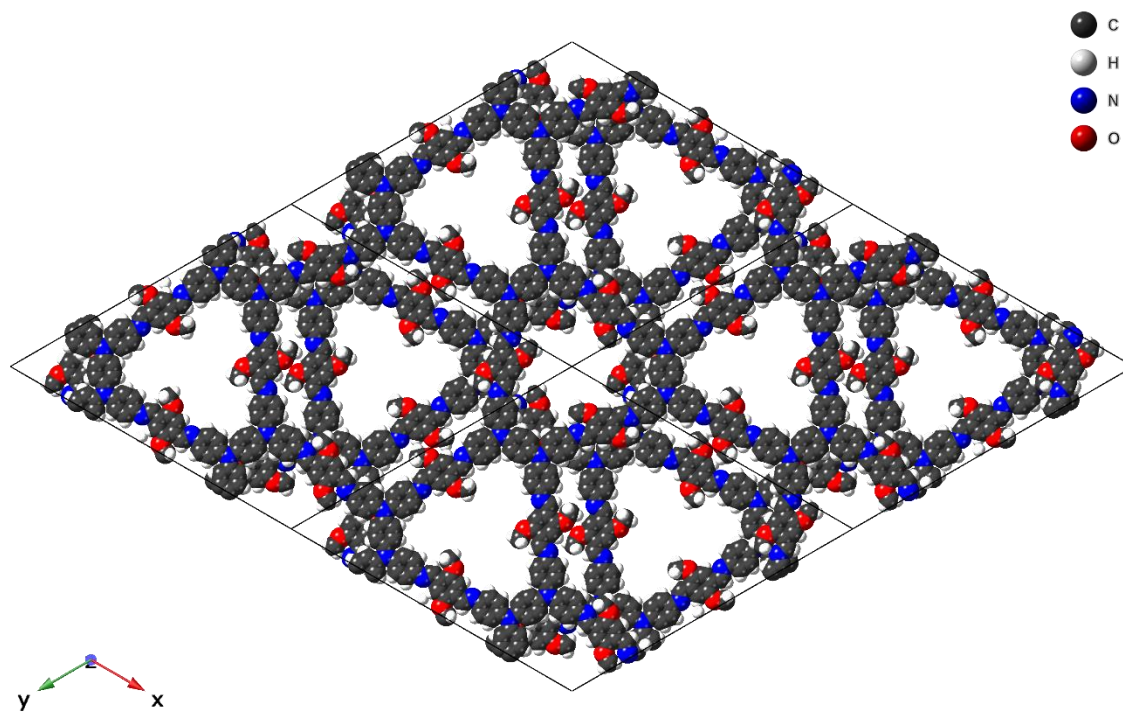
Figure S26: Theoretical structure of TAPD-(Me)$_2$ COF with eclipsed (AB) stacking arrangement.

5. Section S5: Computational modelling

S5.1. Constructing system-specific force fields: To derive system-specific force fields for the two periodic COF materials, *ab initio* calculations were performed on finite molecular clusters using the B3LYP [S4-S6] exchange-correlation functional and the 6-311++G(d,p) Pople basis set [S7] as implemented in the Gaussian16 suite.[S8] Furthermore, the default convergence criteria for distances and angles were adopted (maximum force=0.00045 Ha/a_0 and Ha/rad, rms force=0.00030 Ha/a_0 and Ha/rad, maximum displacement=0.00180 Ha/a_0 and Ha/rad, rms displacement=0.00120 Ha/a_0 and Ha/rad). The pairwise combinations of these molecular systems are representative of the periodic materials as shown in the insets of Figure S27. As such, four different clusters are considered: two ditopic building units corresponding to the linear linker and two tetratopic building units corresponding to the *N,N,N',N'*-Tetrakis(4-aminophenyl)-1,4-phenylenediamine linker, each with a suitable termination to mimic the environment of the moiety in the periodic framework.
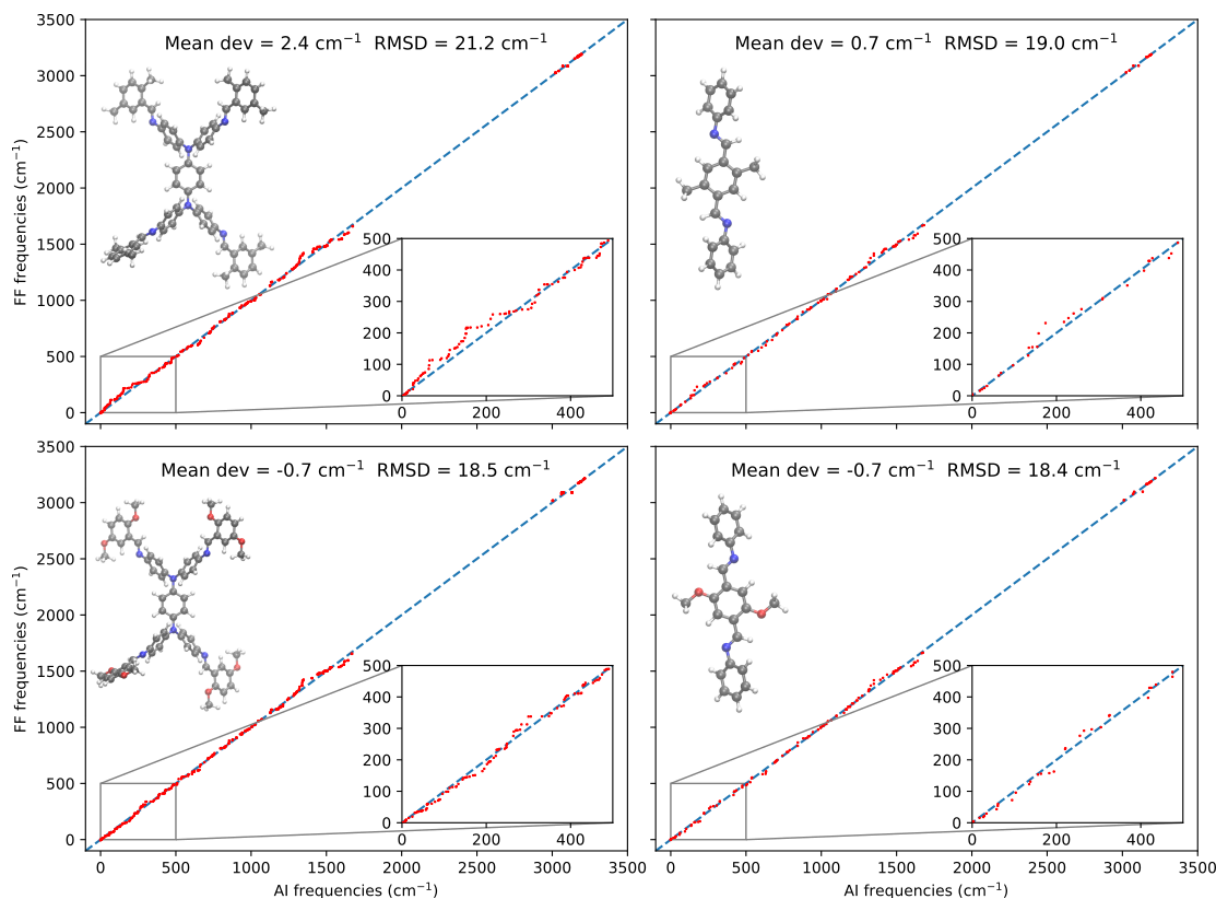
Figure S27: Comparison of the *ab initio* (AI) and force field (FF) normal mode frequencies for all the considered building blocks. The corresponding building block is visualized in the top left corner, with a zoomed-in picture for the low frequencies in the bottom right corner. The dashed lines indicate a perfect agreement.

After optimizing the geometry and calculating the Hessian, a normal mode analysis was performed to confirm that only positive frequencies were present, validating the geometry as a minimum on the potential energy surface. Subsequently, the atomic partial charges were derived using the MBIS partitioning scheme[S9], as implemented in Horton.[S10] Finally, with the optimized geometry, the Hessian and the partial charges as input, QuickFF [S11,S12] was used to derive the covalent force field parameters for the separate clusters. The obtained force fields were then validated with respect to the *ab initio* derived Hessian using TAMkin[S13], yielding good agreement between the force field and *ab initio* frequencies (Fig. S27). Finally, these cluster force fields were combined into force fields for the periodic structures, and a van der Waals model is added *a posteriori*, modeled by the MM3-Buckingham potential.[S14] The resulting force fields are provided as part of the Supplementary Information.

S5.2. Structural models: While the AA and AB stacking models of Section S4 account for the different relative positions of adjacent layers, the relative position of the functional groups in adjacent layers forms an additional degree of freedom that can influence the geometry of the COFs and hence their PXRD patterns. To take this into account, we constructed two different stacking models with varying locations of the functional groups across the layers, as illustrated in Figure S28. The configuration with aligned functional groups is labelled as 'parallel', while the configuration with alternating locations is labelled 'inverted'. These parallel and inverted models are considered

separately from the AA and AB stacking models mentioned before. As our simulations allow for layer movement, there is no need to consider the AA and offsetted AB configuration as distinct models.
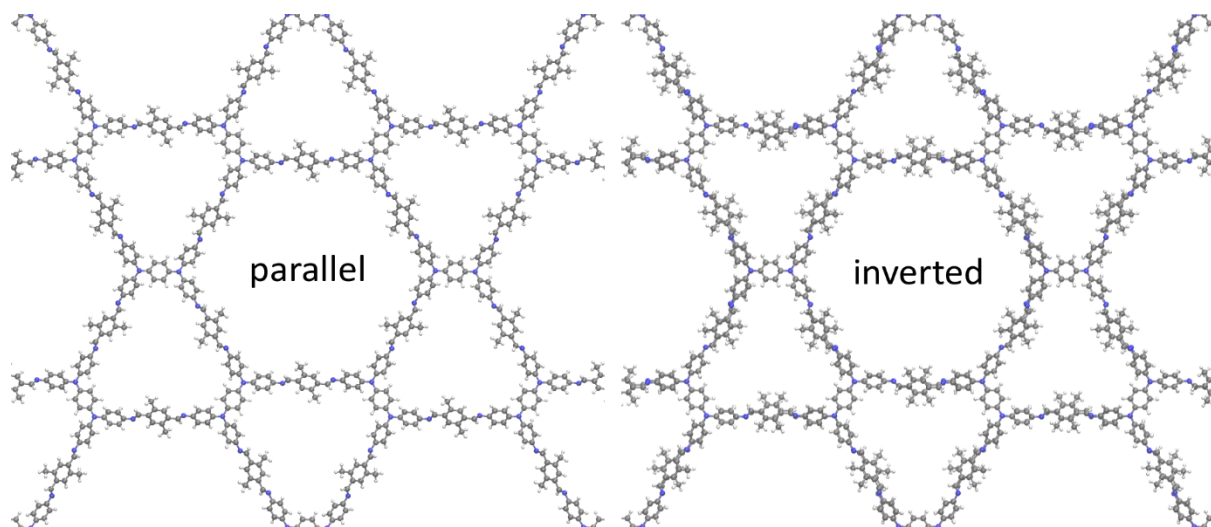
Figure S28: The parallel and inverted structural models used for TAPD-(Me)$_2$, with analogous models adopted for TADP-(OMe)$_2$. (Left) In the parallel model, the location of the functional groups is identical in all layers. (Right) In the inverted model, the location of the functional groups alternates across adjacent layers.

S5.3. Generation of computational PXRD patterns: An accurate description of the potential energy surface (PES) and its sampling are essential when calculating a computationally representative diffraction pattern. In a first approach, we followed a static approach to sample the PES by optimizing the different structural models at zero Kelvin. The resulting PXRD patterns and their relative agreement with the experimentally observed patterns are visualized in Figure S29 and show already good correspondence. The PXRD patterns were calculated employing the pyobjcryst python package, based on the ObjCryst++ Object-Oriented Crystallographic Library. [S15] In accordance with experiment, the Cu K$_\alpha$ wavelength of 1.54056 Å was used. The peak shape was calculated using a pseudo-Voigt shape function, with mixing parameter $\eta = \eta_0 + \eta_1\, 2\theta + \eta_2\, 2\theta^2$ (η_0= 0.5, η_1 = 0, η_2 = 0) which determines the ratio between Lorentzian and Gaussian shape functions. The corresponding peak width, $H^2 = U \tan^2(\theta) + V \tan(\theta) + W$, is fixed with W=0.02 degrees, keeping the other parameters U, V equal to 0 degrees.
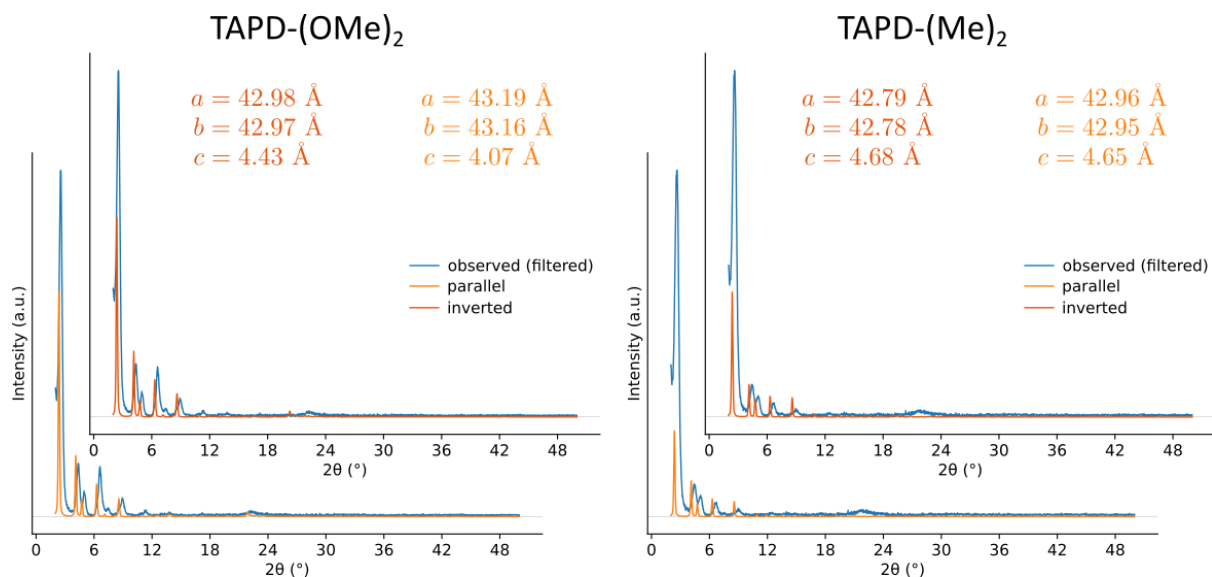
Figure S29: Comparison between the observed and calculated PXRD patterns, and the derived unit cell parameters, based on the force field optimized structures of TAPD-$(OMe)_2$ and TAPD-$(Me)_2$.

However, at elevated temperatures and pressures, the reflection planes will show small dynamic fluctuations over time that increase with increasing temperature due to atomic vibrations. Inherently, an XRD measurement thus provides a time-averaged view of these dynamic reflection planes at certain operando conditions. To mimic these dynamic effects, in our second approach, we performed MD simulations and took different snapshots from the resulting trajectories. Here, Yaff[S16] was used as the MD engine and interfaced with LAMMPS[S17] to efficiently compute the long-range interactions. A time step of 0.5 fs was used with a run time of 400 ps taking a snapshot every 0.1 ps. The MD simulations were performed in the $(N,P,\pmb{\sigma}_a=\pmb{0},T)$ ensemble[S18], fixing the temperature at 300 K with a Nosé-Hoover chain thermostat[S19-S21] with three beads and a relaxation time of 100 fs. The pressure was controlled at 1 bar by a Martyna-Tuckerman-Tobias-Klein barostat[S22, S23] with a relaxation time of 1000 fs. As a result, this second approach allows for an *ab initio* protocol to introduce average atomic displacements into the computationally derived PXRD patterns, as these snapshots are generated using an *ab initio* derived force field, accounting for temperature effects that were missing in the first approach. Time-averaging the PXRD pattern over the course of the simulation thus provides a more accurate representation of the atomic structure during measurement, generally resulting in a better correspondence with experimentally observed PXRD patterns. This is indeed observed in Figure S30, showing excellent agreement between the experimental and the MD averaged diffraction patterns.
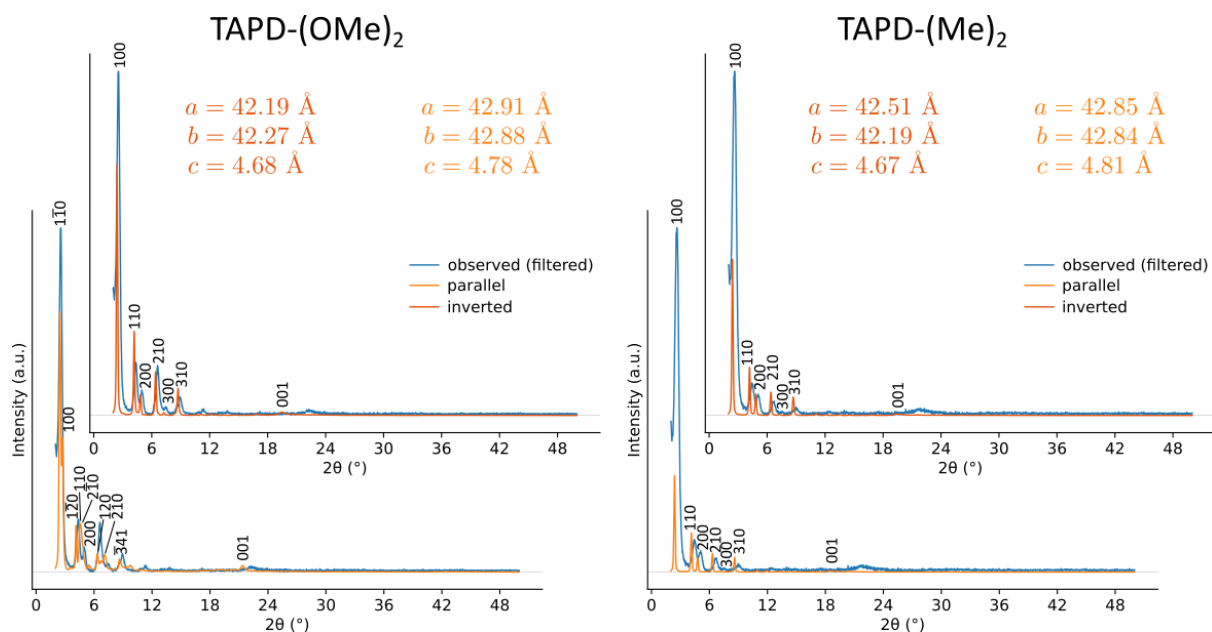
Figure S30: Comparison between the observed and calculated PXRD patterns, and the unit cell parameters, based on the molecular dynamics simulations of TAPD-(OMe)$_2$ and TAPD-(Me)$_2$.

S5.4. Stacking offset: As our MD simulations can dynamically switch between AA and AB stackings, they directly reveal the preferred alignment between adjacent layers, as quantified by their offset (Figure S31). From our MD simulations, it is apparent that, for both COFs, the offsets between adjacent layers is very limited and without directionality, such that the average structure during the MD simulation resembles a 2D COF with an eclipsed (AA) stacking (Figure S31).
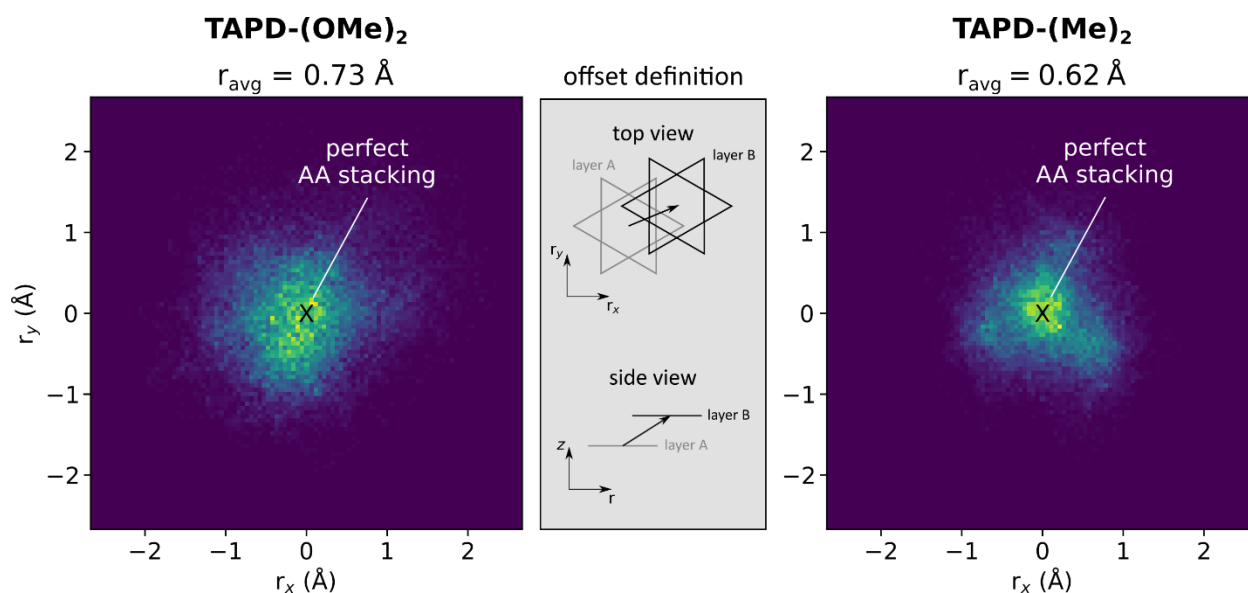
Figure S31: Heatmap of the offsets between adjacent layers for (Left) TAPD-(OMe)$_2$ and (Right) TAPD-(Me)$_2$. The average offset with respect to perfect AA stacking, r_{avg}, is reported at the top of each heatmap.

S22

6. Section S6: Gas sorption

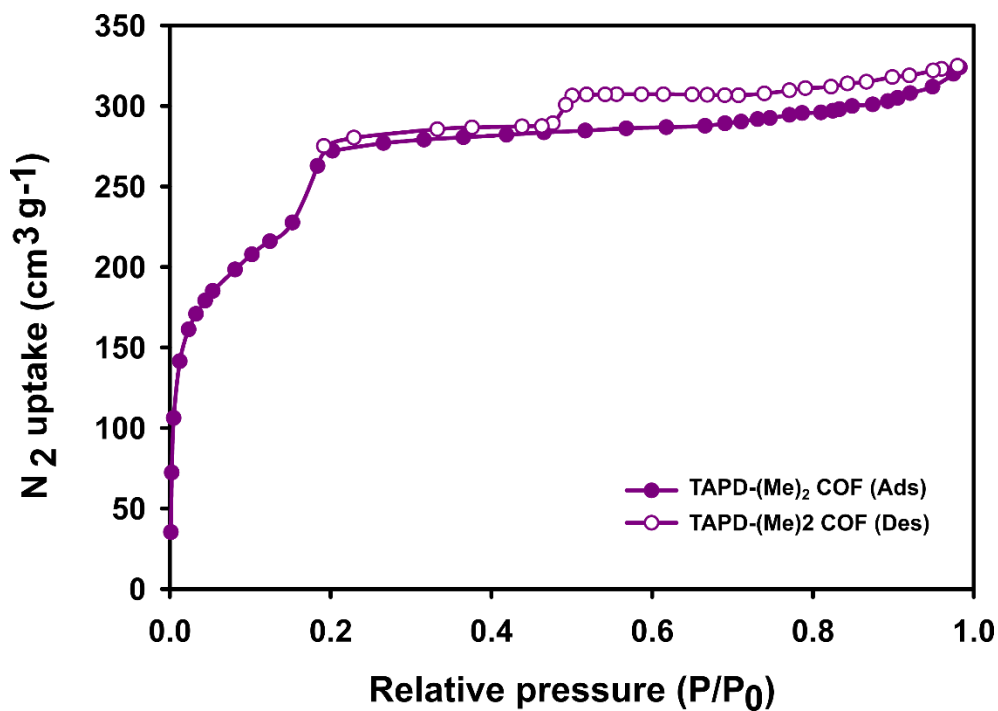**Figure S32:** N$_2$ sorption isotherms of TAPD-(Me)$_2$ COF.
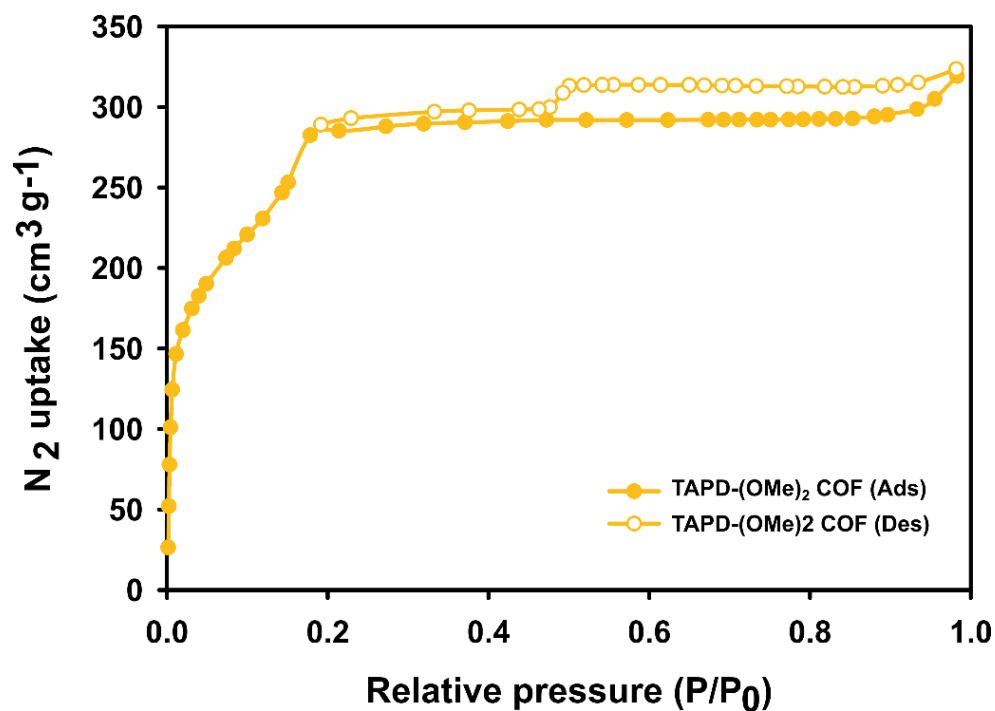

**Figure S33:** N$_2$ sorption isotherms of TAPD-(OMe)$_2$ COF.

7. Section S7: Photo(electro)chemical characterization and photocatalytic experiment details

S7.1. Photo(electro)chemical characterization: For the electrochemical measurements, a thin layer of COF was deposited on FTO. To this end, 2 mg of COF was dispersed in a mixture of 350 µl acetonitrile, 150 µl tetrahydrofuran, 100 µl trifluoroacetic acid (TFA) and 20 µl water. The TFA temporarily protonates the imine bonds, which positively charges the COF layers, strongly increasing their electrostatic repulsion, which in turn leads to improved dispersion behavior [S24]. The mixture was sonicated for 1 hour until a visually homogeneous dispersion was obtained. 100 µl of this dispersion was drop-casted on a 1 cm × 2 cm area of an FTO substrate. After drying, the coating was soaked in ethanol for two minutes, which deprotonated the COF layer. This could be visually observed as a fast change in color (Fig. S34), accompanied by the formation of small H_2 gas bubbles. The coating was left to dry under air for one hour.
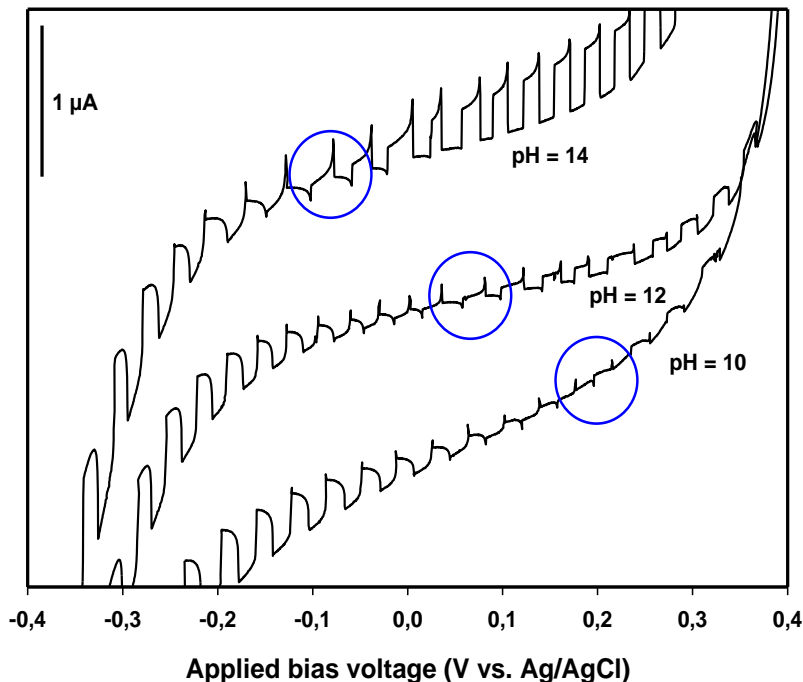

Figure S34: The photocatalyst-coated FTO substrate before (left) and after (right) soaking in ethanol.
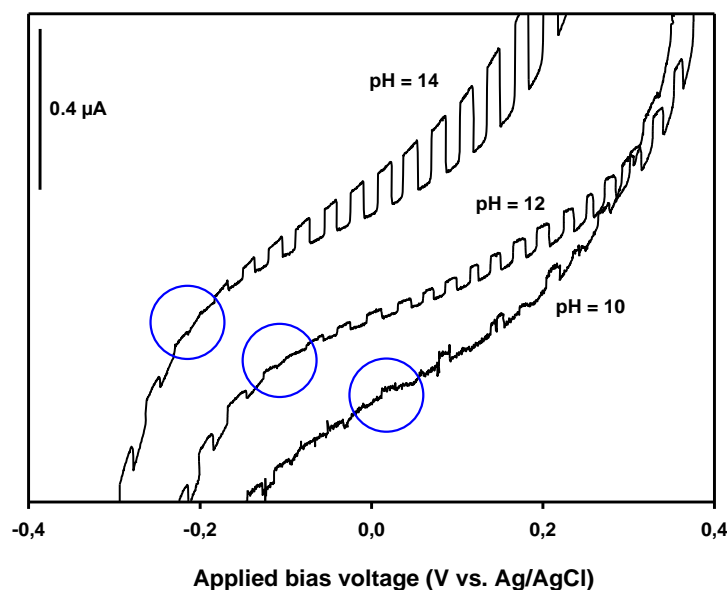
Figure S35: TAPD-(Me)$_2$ COF. Linear sweep voltammetry under chopped illumination in three electrolytes with different pH. The potential regions where the photocurrent changes its sign are marked in blue.

Figure S36: TAPD-(OMe)$_2$ COF. Linear sweep voltammetry under chopped illumination in three electrolytes with different pH. The potential regions where the photocurrent changes its sign are marked in blue.

Photoelectrochemical measurements were performed in either 1 M NaOH (pH = 14), 0.2 M KCl/NaOH buffer (pH = 12) or 0.06 M Na$_2$B$_4$O$_7$.10H$_2$O/NaOH buffer (pH = 10) using an ALS-Japan Ag/AgCl 3 M NaCl reference electrode (+0.195 V vs. SHE), an ALS-Japan Pt coil counter electrode and the photocatalyst-coated FTO as working electrode. 5 ml electrolyte was used, so that the entire photocatalyst-coated surface of the FTO substrate was submerged. The electrolyte was de-aerated with Ar before every measurement. We found that measurements in acidic electrolytes (pH < 7) gave less reproducible results.

Measurements were recorded using a Bio-Logic VSP potentiostat and EC-Lab software. White light was provided by a Philips Tornado T2 CFL (23 W, 1450 lumen). The voltage was swept in the negative direction from +0.4 V to -0.4 V vs. Ag/AgCl at a scanrate of 4 mV/s, whilst at the same time the white light was chopped every 3 seconds.

The potential at which the photocurrent sign change occurred was visually determined from the LSV curves, and from here on will be referred to as the Umklapppotential, E$_{UK}$ (Fig. S35 and S36). The redox potential of the electrolyte E$_{electrolyte}$ (V vs. Ag/AgCl) was calculated from the pH according to:

$$E_{electrolyte} = -0.195 - 0.059 \times pH$$

The difference in E$_{UK}$ and E$_{electrolyte}$ is the voltage bias that is necessary to align the electrolyte potential with the conduction band minimum (Fig. S37). Therefore, the conduction band minimum E$_{CBM}$ (V. vs Ag/Ag/Cl) can be found at an energy level that is $(E_{UK}-E_{electrolyte})$ volts more negative than the redox potential of the electrolyte E$_{electrolyte}$.

$$E_{CBM} = E_{electrolyte} - \left(E_{UK} - E_{electrolyte}\right) = 2E_{electrolyte} - E_{UK}$$
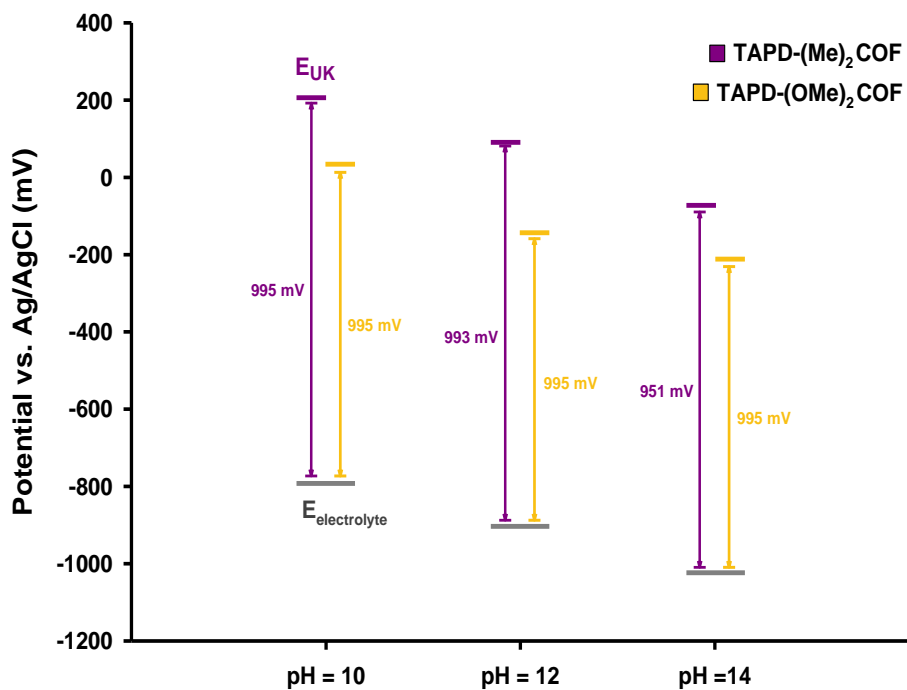
Figure S37: Electrolyte redox potentials $E_{electrolyte}$ and Umklappotentials E_{UK} of TAPD-$(Me)_2$ COF and TAPD-$(OMe)_2$ COF.

The calculated conduction band minima follow a Nernstian dependence in good approximation. From the values at pH 14, 12 and 10, we extrapolated a value for the conduction band minimum at pH = 0 (Fig. S38).

pH	$E_{electrolyte}$ vs. Ag/AgCl (mV)	E_{UK} vs. Ag/AgCl (mV) TAPD-$(Me)_2$ COF	E_{UK} vs. Ag/AgCl (mV) (TAPD-$(OMe)_2$ COF
14	-1021	-70	-210
12	-903	90	-140
10	-785	210	30

pH	E_{CBM} vs. NHE (mV) TAPD-$(Me)_2$ COF	E_{CBM} vs. NHE (mV) (TAPD-$(OMe)_2$ COF
14	-1777	-1637
12	-1701	-1471
10	-1585	-1405
0	-972	-796
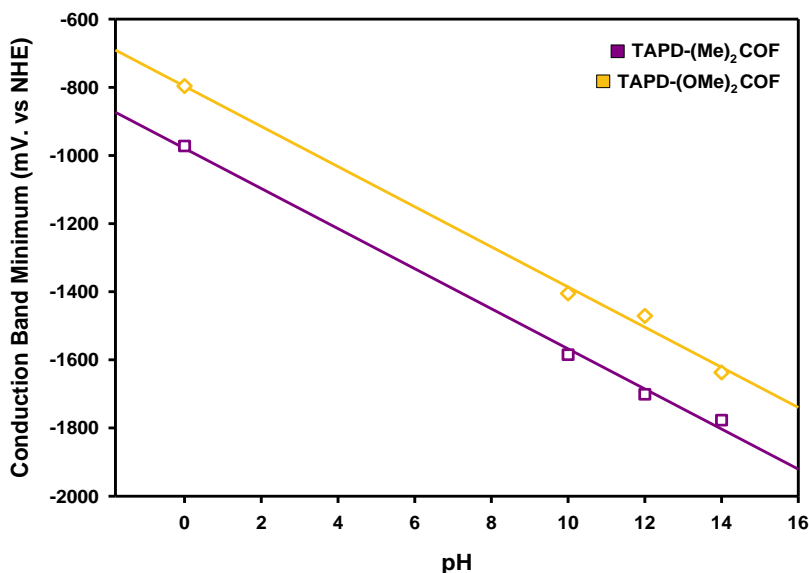
Figure S38: The measured conduction band minima at pH = 10, pH = 12 and pH = 14 approximately follow a Nernstian dependence. The conduction band minima at pH = 0 were extrapolated from these values.

S7.2. Photocatalytic experiment details: Hydrogen peroxide production was carried out in 15 ml glass vial. 20 mg of catalyst was dispersed in 5 mL water:ethanol (9:1) mixture and sonicated for 5 minutes. Oxygen gas was saturated in the mixture for 20 minutes by bubbling and vial was sealed. 250W lamp within 420-700nm wavelength was irradiated on the vial in a dark room (light intensity = 5.46 W.m^{-2}). The temperature was maintained at 25°C using a condenser. The distance between the reactor and the light source was kept fixed at 15 cm and stirring speed was maintained at 900 rpm. After the reaction, the products were analyzed by iodometric titration to determine hydrogen peroxide concentration. Selectivity = $[H_2O_2]/([RCHO] + [RCOOH]) \times 100$
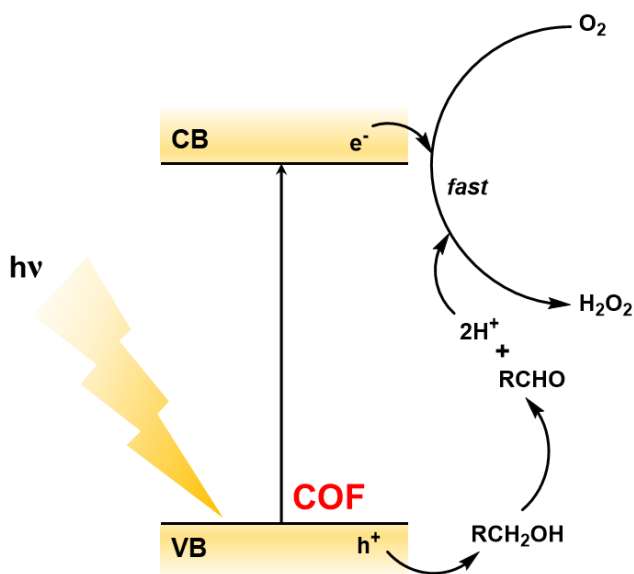
Figure S39: Proposed mechanism for the photocatalytic formation of hydrogen peroxide.
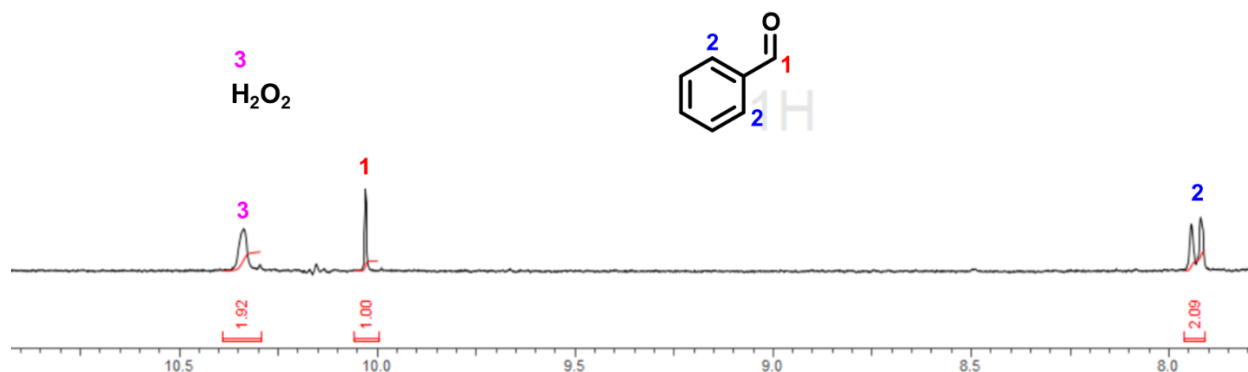
Figure S40: ^{1}H NMR spectra of the end product (crude) after 16 h reaction with water:benzylalcohol (1:9) at room temperature using TAPD-(Me)$_2$ COF. Mesitylene of known concentration was used to quantify the amount of benzyl alcohol and H$_2$O$_2$ produced. [RCHO] = 56 μmol, [H$_2$O$_2$] = 53.7 μmol, [RCOOH] = 0 μmol (not detected in NMR and GC-MS).

Table S3: Photocatalytic results under various conditions.

Entry	Photocatalyst	Solvent system	Gas	Irradiation conditions	H$_2$O$_2$ produced (μmol)
1.	Model Compound TAPD-(Me)$_2$-MC	Water:EtOH (9:1)	O$_2$ saturated	λ = 420-700 nm	7
2.	Blank	Water:EtOH (9:1)	O$_2$ saturated	λ = 420-700 nm	-
3.	TAPD-(Me)$_2$ COF	Water:EtOH (9:1)	O$_2$ saturated	Dark	-
4.	TAPD-(Me)$_2$ COF	Water:Benzylalcohol (1:9)	O$_2$ saturated	λ = 420-700 nm	53.7
5.	TAPD-(Me)$_2$ COF	Water:EtOH (9:1)	Ambient	λ = 420-700 nm	8
6.	TAPD-(Me)$_2$ COF	Water:EtOH (9:1), 4 days	O$_2$	λ = 420-700 nm	142.3
7.	TAPD-(Me)$_2$ COF	Water:EtOH (9:1)	Triethylamine (TEA): h$^+$ trapping agent	λ = 420-700 nm	-
8.	TAPD-(Me)$_2$ COF	Water:EtOH (9:1)	AgNO$_3$: e$^-$ trapping agent	λ = 420-700 nm	2
9.	TAPD-(Me)$_2$ COF	Water:EtOH (9:1)	Benzoquinone: Radical scavenger	λ = 420-700 nm	22

S7.3. Recyclability test: TAPD-(Me)$_2$ COF was collected after each run through filtration and washed thoroughly with acetone and THF. Before performing the second run, it was dried under vacuum at 120°C for 12 hours.
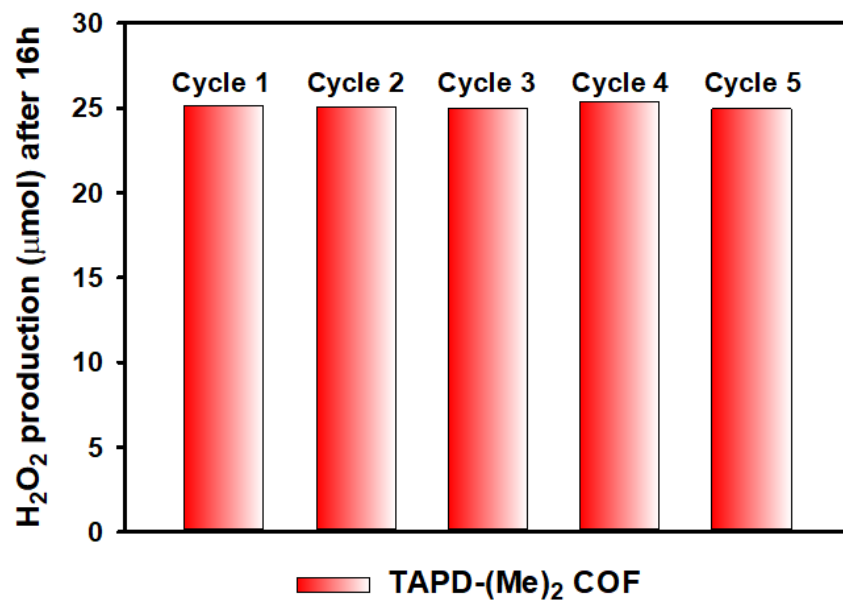
Figure S41: H_2O_2 production for 5 consecutive cycles using TAPD-$(Me)_2$ COF.
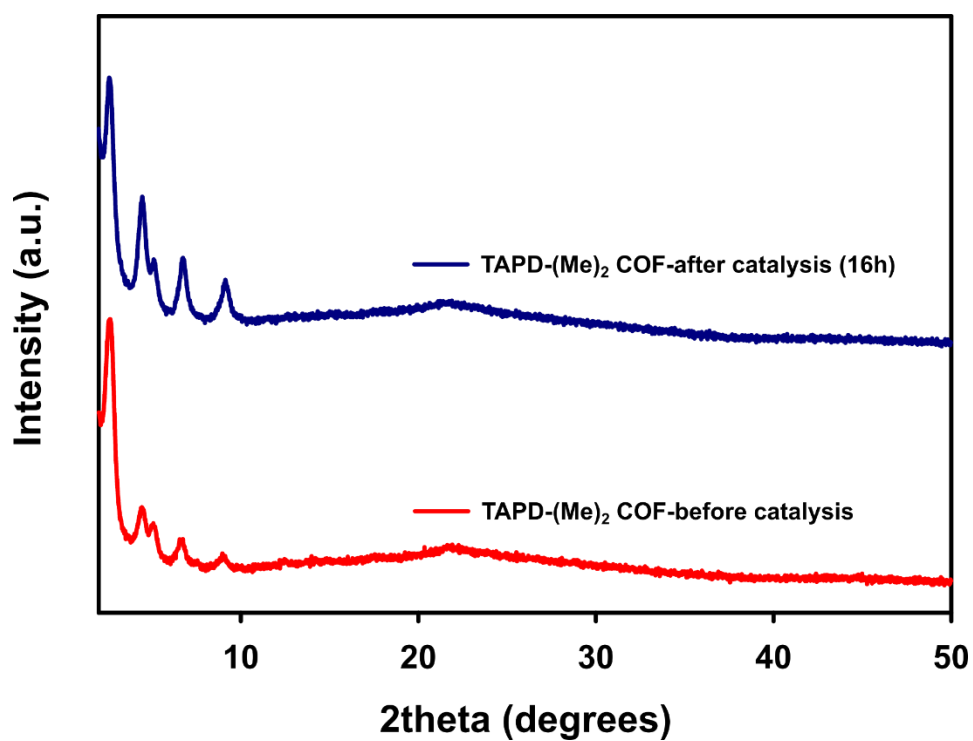
Figure S42: PXRD patterns of TAPD-$(Me)_2$ COF before and after catalysis showing that the crystallinity is retained.
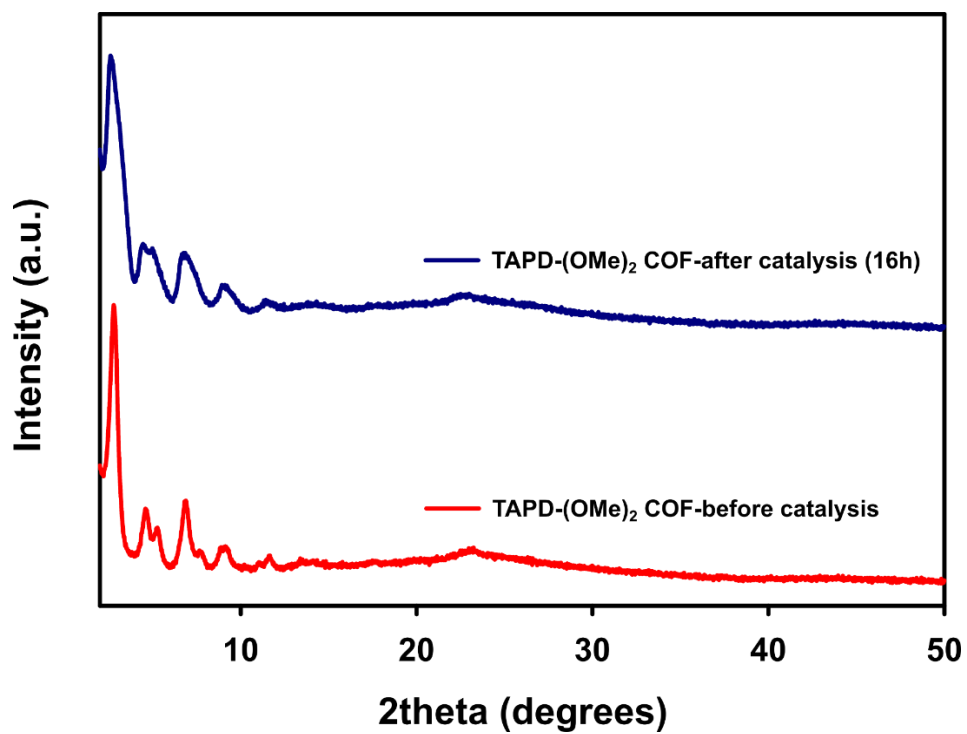
Figure S43: PXRD patterns of TAPD-(OMe)$_2$ COF before and after catalysis showing that the crystallinity is retained.
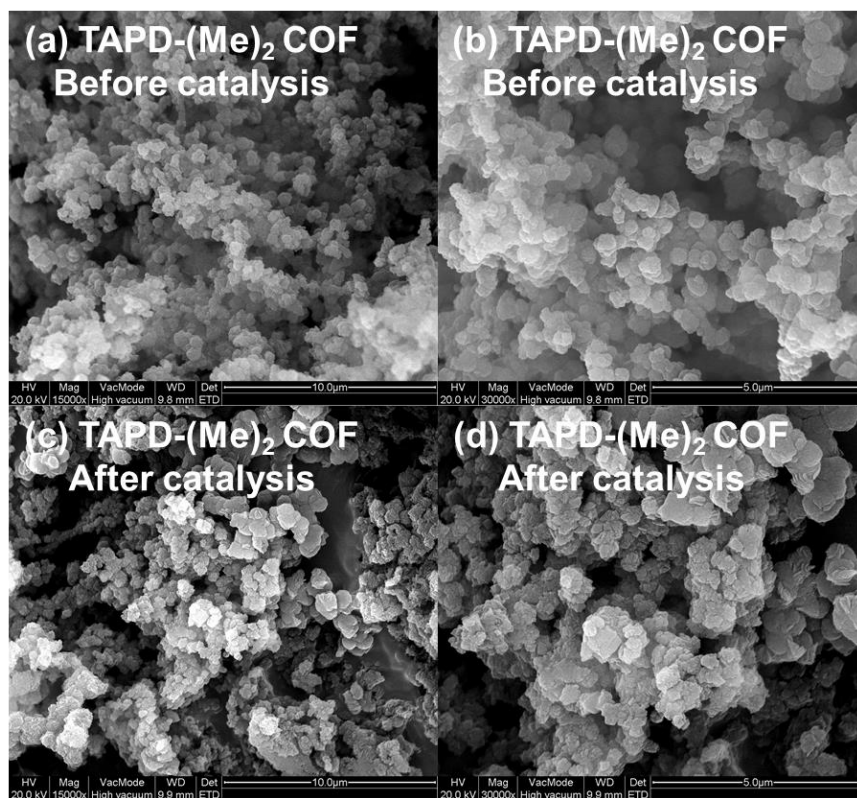
Figure S44: SEM images of TAPD-(Me)$_2$ COF before and after catalysis.

Figure S45: SEM images of TAPD-(OMe)$_2$ COF before and after catalysis.

Figure S46: Production of H$_2$O$_2$ vs time.

Figure S47: Effect of different proton donors in the overall production

of H_2O_2.

8. <u>Section S8: References</u>

S1. Chandran, C.V.; Madhu, P.K.; Kurur, N.D.; Bräuniger, T. Swept-frequency two-pulse phase modulation (SWf-TPPM) sequences with linear sweep profile for heteronuclear decoupling in solid-state NMR. *Magn. Reson. Chem.* 2008, *46*(10) 943-947.
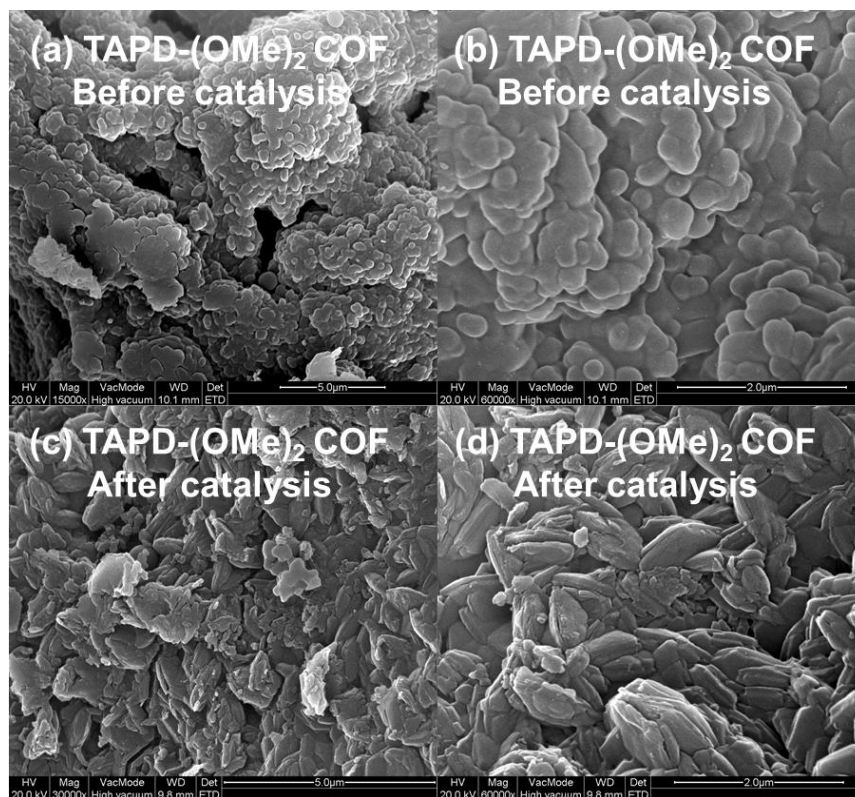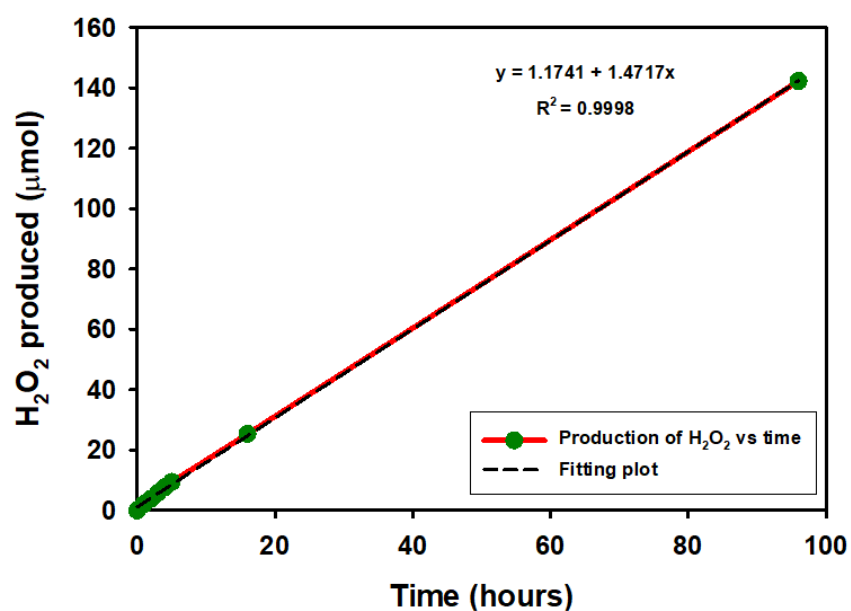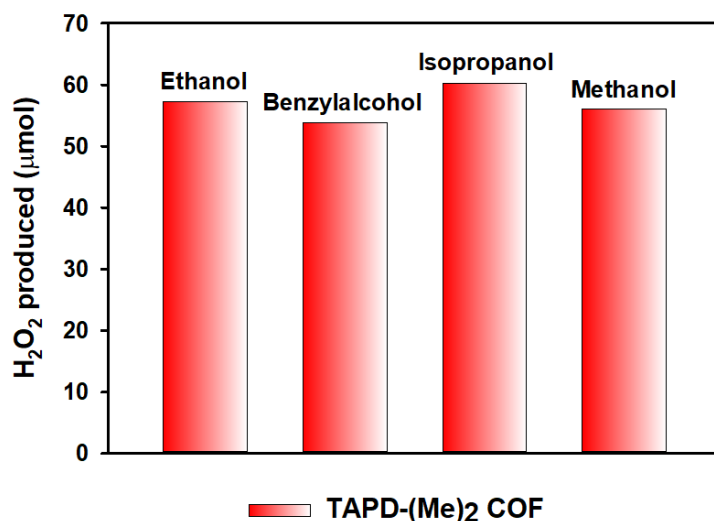
S2. Feike, M.; Demco, D.E.; Graf, R.; Gottwald, J.; Hafner, S.; Spiess, H.W. Broadband multiple-quantum NMR spectroscopy. *J. Magn. Reson. Ser. A* 1996, *122*(2), 214-221.

S3. Graf, R.; Demco, D.E.; Gottwald, J.; Hafner, S.; Spiess, H.W. Dipolar couplings and internuclear distances by double-quantum nuclear magnetic resonance spectroscopy of solids. *J. Chem. Phys.* 1997, *106*(3), 885-895.

S4. Becke, A. D. Density-functional thermochemistry. III. The role of exact exchange. *J. Chem. Phys.* 1993, 98, 5648–5652.

S5. Lee, C.; Yang, W.; Parr, R. G. Development of the Colle-Salvetti correlation-energy formula into a functional of the electron density. *Phys. Rev. B* 1988, 37, 785–789.

S6. Stephens, P. J.; Devlin, F. J.; Chabalowski, C. F.; Frisch, M. J. Ab initio calculation of vibrational absorption and circular dichroism spectra using density functional force fields. *J. Chem. Phys.* 1994, 98, 11623–11627.

S7. Frisch, M. J.; Pople, J. A.; Binkley, J. S. Self-consistent molecular orbital methods 25. Supplementary functions for Gaussian basis sets. *J. Chem. Phys.* 1984, 80, 3265–3269.

S8. Frisch, M. J. et al. Gaussian 16 Revision A.03. 2016; Gaussian Inc. Wallingford CT.

S9. Verstraelen, T.; Vandenbrande, S.; Heidar-Zadeh, F.; Vanduyfhuys, L.; Van Speybroeck, V.; Waroquier, M.; Ayers, P. W. Minimal Basis Iterative Stockholder: Atoms in Molecules for Force-Field Development. *J. Chem. Theory Comput.* 2016, 12, 3894–3912.

S10. Verstraelen, T.; Tecmer, P.; Heidar-Zadeh, F.; Boguslawski, K.; Chan, M.; Zhao, Y.; Kim, T. D.; Vandenbrande, S.; Yang, D.; González-Espinoza, C. E.; Fias, S.; Limacher, P. A.; Berrocal, D.; Malek, A.; Ayers, P.

W. HORTON 2.0.0. 2015; http://theochem.github.com/horton/.

S11. Vanduyfhuys, L.; Vandenbrande, S.; Verstraelen, T.; Schmid, R.; Waroquier, M.; Van Speybroeck, V. QuickFF: A program for a quick and easy derivation of force fields for metal-organic frameworks from ab initio input. *J. Comput. Chem.* 2015, 36, 1015–1027.

S12. Vanduyfhuys, L.; Vandenbrande, S.; Wieme, J.; Waroquier, M.; Verstraelen, T.; Van Speybroeck, V. Extension of the QuickFF force field protocol for an improved accuracy of structural, vibrational, mechanical and thermal properties of metal-organic frameworks. *J. Comput. Chem.* 2018, 39, 999–1011.

S13. Ghysels, A.; Verstraelen, T.; Hemelsoet, K.; Waroquier, M.; Van Speybroeck, V. TAMkin: a versatile package for vibrational analysis and chemical kinetics. *J. Chem. Inf. Model.* 2010, 50, 1736–1750.

S14. Allinger, N. L.; Yuh, Y. H.; Lii, J.-H. Molecular mechanics. The MM3 force field for hydrocarbons. 1. *J. Am. Chem. Soc.* 1989, 111, 8551–8566.

S15. Favre-Nicolin, V.; Černý, R. FOX, `free objects for crystallography': a modular approach to ab initio structure determination from powder diffraction. *J. Appl. Cryst.* 2002, 35, 734–743.

S16. Verstraelen, T.; Vanduyfhuys, L.; Vandenbrande, S.; Rogge, S. M. J. Yaff, yet another force field. http://molmod.ugent.be/software/.

S17. Plimpton, S. Fast Parallel Algorithms for Short-Range Molecular Dynamics. *J. Comput. Phys.* 1995, 117, 1–19.

S18. Rogge, S. M. J.; Vanduyfhuys, L.; Ghysels, A.; Waroquier, M.; Verstraelen, T.; Maurin, G.; Van Speybroeck, V. A Comparison of Barostats for the Mechanical Characterization of Metal-Organic Frameworks. *J. Chem. Theory Comput.* 2015, 11, 5583–5597.

S19. Nosé, S. A molecular dynamics method for simulations in the canonical ensemble. *Mol. Phys.* 1984, 52, 255–268.

S20. Hoover, W. G. Canonical dynamics: Equilibrium phase-space distributions. *Phys. Rev. A* 1985, 31, 1695–1697.

S21. Martyna, G. J.; Klein, M. L.; Tuckerman, M. Nosé-Hoover chains: The canonical ensemble via continuous dynamics. *J. Chem. Phys.* 1992, 97, 2635–2643.

S22. Martyna, G. J.; Tobias, D. J.; Klein, M. L. Constant pressure molecular dynamics algorithms. *J. Chem. Phys.* 1994, 101, 4177–4189.

S23. Martyna, G. J.; Tuckerman, M. E.; Tobias, D. J.; Klein, M. L. Explicit reversible integrators for extended systems dynamics. *Mol. Phys.* 1996, 87, 1117–1157.

S24. Burke, D. W.; Sun, C.; Castano, I.; Flanders, N. C.; Evans, A. M.; Vitaku, E.; Mcleod, D. C.; Lambeth, R. H.; Chen, L. X.; Gianneschi, N. C.; Dichtel, W. R. Acid Exfoliation of Imine-linked Covalent Organic Frameworks Enables Solution Processing into Crystalline Thin Films. *Angew. Chemie Int. Ed.* 2020, 59, 5165–5171.